

# On the Southern Hemisphere Stratospheric Response to ENSO and Its Impacts on Tropospheric Circulation

KANE A. STONE,<sup>a</sup> SUSAN SOLOMON,<sup>a</sup> DAVID W. J. THOMPSON,<sup>b</sup> DOUGLAS E. KINNISON,<sup>c</sup> AND JOHN C. FYFE<sup>d</sup>

<sup>a</sup> *Department of Earth, Atmospheric, and Planetary Sciences, Massachusetts Institute of Technology, Cambridge, Massachusetts*

<sup>b</sup> *Department of Atmospheric Science, Colorado State University, Fort Collins, Colorado*

<sup>c</sup> *Atmospheric Chemistry Observations and Modeling Laboratory, National Center for Atmospheric Research, Boulder, Colorado*

<sup>d</sup> *Canadian Centre for Climate Modelling and Analysis, Environment and Climate Change Canada, Victoria, British Columbia*

(Manuscript received 29 March 2021, in final form 28 November 2021)

**ABSTRACT:** As the leading mode of Pacific variability, El Niño–Southern Oscillation (ENSO) causes vast and widespread climatic impacts, including in the stratosphere. Following discovery of a stratospheric pathway of ENSO to the Northern Hemisphere surface, here we aim to investigate if there is a substantial Southern Hemisphere (SH) stratospheric pathway in relation to austral winter ENSO events. Large stratospheric anomalies connected to ENSO occur on average at high SH latitudes as early as August, peaking at around 10 hPa. An overall colder austral spring Antarctic stratosphere is generally associated with the warm phase of the ENSO cycle, and vice versa. This behavior is robust among reanalysis and six separate model ensembles encompassing two different model frameworks. A stratospheric pathway is identified by separating ENSO events that exhibit a stratospheric anomaly from those that do not and comparing to stratospheric extremes that occur during neutral ENSO years. The tropospheric eddy-driven jet response to the stratospheric ENSO pathway is the most robust in the spring following a La Niña, but extends into summer, and is more zonally symmetric compared to the tropospheric ENSO teleconnection. The magnitude of the stratospheric pathway is weaker compared to the tropospheric pathway and therefore, when it is present, has a secondary role. For context, the magnitude is approximately half that of the eddy-driven jet modulation due to austral spring ozone depletion in the model simulations. This work establishes that the stratospheric circulation acts as an intermediary in coupling ENSO variability to variations in the austral spring and summer tropospheric circulation.

**KEYWORDS:** ENSO; Stratosphere; Stratosphere-troposphere coupling

## 1. Introduction

Southern Hemisphere (SH) tropospheric climate variability is connected to El Niño–Southern Oscillation (ENSO), particularly during the austral summer period. Additionally, strong ENSO events are also known to impact the stratospheric circulation, predominantly in the Northern Hemisphere (NH) winter, and subsequently providing a “stratospheric pathway” onto NH surface climate (Butler et al. 2014; Domeisen et al. 2019). This leads to the questions: To what extent does austral winter ENSO also modulate the SH austral spring stratosphere? And does the SH stratosphere provide a pathway through which ENSO variability influences the SH tropospheric circulation?

Sea surface temperature (SST) variability in the tropical Pacific region is dominated by ENSO (Bjerknes 1969; Wyrski 1975; Rasmusson and Carpenter 1982). The classic ENSO description is the leading mode of variability in tropical Pacific SSTs. The ENSO events typically begin in June–August, peak in December–March, and diminish by April–May (Trenberth 1997). They have far-reaching global weather impacts, commonly referred to as teleconnections (Bjerknes

1969; Liu and Alexander 2007; Horel and Wallace 1981). For example, El Niño and La Niña events are associated with a disruption in the Walker circulation, a tropical Pacific zonal circulation pattern (Lindzen and Nigam 1987), causing changes in rainfall in both Australia (e.g., McBride and Nicholls 1983; King et al. 2015) and the Americas (e.g., Grimm and Tedeschi 2009; Ropelewski and Halpert 1986).

In the SH, ENSO is linked to the South Pacific convergence zone (SPCZ), a band of convection in the South Pacific (Trenberth 1984), and the Pacific–South American (PSA) pattern, a quasi-stationary Rossby wave train emanating from the equatorial Pacific toward the southeast Pacific and then equatorward in the Atlantic (Karoly 1989; Mo and Ghil 1987; Mo and Paegle 2001). Interannual variability of the tropospheric circulation in the SH is linked to the PSA (Garreaud and Battisti 1999). Further, SH regional variability within 180°–360°E is dominated by two quasi-stationary anticyclones with strengths that are negatively correlated to the PSA (Hobbs and Raphael 2010). The occurrence of blocking over the South Pacific, along the PSA track, is modulated strongly by ENSO (Renwick 1998; Renwick and Revell 1999). Recent studies have also suggested that the PSA may represent part of the zonal asymmetric structure of the southern annular mode (SAM) (Irving and Simmonds 2016). Therefore, the connection of ENSO to SH circulation is notable, especially in the South Pacific region.

While ENSO is the leading mode of variability in the tropics, the SAM is a leading mode of variability within the

Supplemental information related to this paper is available at the Journals Online website: <https://doi.org/10.1175/JCLI-D-21-0250.s1>.

Corresponding author: Kane A. Stone, [stonek@mit.edu](mailto:stonek@mit.edu)

SH extratropics, and is described as a change in sea level pressure between the SH midlatitudes and polar regions (Kidson 1988; Karoly 1990; Kidson and Sinclair 1995; Hartmann and Lo 1998; Thompson and Wallace 2000). A positive SAM is associated with lower sea level pressure over Antarctica and higher pressure in the midlatitudes, and is strongly coupled to the location of the eddy-driven jet stream and therefore Rossby wave-induced weather fronts (Thompson and Wallace 2000; Lorenz and Hartmann 2001), where a positive SAM denotes a poleward shift of the jet. The connection between ENSO and SAM has widely been documented as negatively correlated, with ENSO projecting strongly onto the SAM (Seager et al. 2003; L'Heureux and Thompson 2006; Fogt et al. 2011; Lim et al. 2013; Wang et al. 2013). However, this relationship may be dependent on the strength of ENSO (Kim et al. 2017). Additionally, Fogt et al. (2012) showed that zonal asymmetries in the SAM during austral spring and summer are closely tied to ENSO, especially in the South Pacific, and can have regional temperature impacts.

A number of studies using different models and approaches have examined the influence of springtime Antarctic ozone depletion that has occurred in the last few decades on the austral summer SAM (Thompson and Solomon 2002; Arblaster and Meehl 2006; Son et al. 2009; Polvani et al. 2011; Thompson et al. 2011). Stratosphere–troposphere coupling in the SH is also known to occur as early as austral spring after wintertime anomalies in the upper stratosphere occur due to planetary wave breaking (Thompson et al. 2005; Lim et al. 2018). This raises the question of linkages between wintertime ENSO and stratospheric ozone impacts on the SAM.

Past studies of ENSO teleconnections into the stratosphere have shown large disturbances in the polar stratosphere temperatures, particularly in the NH and during austral summer (Domeisen et al. 2019 and references therein), the time period when ENSO peaks (Trenberth 1997), and heat transport is largest into the NH stratosphere (e.g., McIntyre and Palmer 1983). In the SH, central Pacific (where the large SST anomalies are located farther west) El Niño events have been shown to have a large impact on the SH stratosphere due to a more enhanced Rossby wave train along the SPCZ (Hurwitz et al. 2011; Yang et al. 2015; Domeisen et al. 2019). Hurwitz et al. (2011) showed that September–November eastern Pacific El Niño had little impact on the SH stratosphere, while Simpson et al. (2011) reported a strong response in the SH midlatitudes during austral summer. A recent study suggested that correlations between ENSO and the SH stratosphere are largest a year after an ENSO event, and typically display a dipole structure between the upper and lower stratosphere (Lin and Qian 2019), whereas other studies have showed a lag correlation between the SH spring stratosphere and the previous June central tropical Pacific SST variability (Evtushevsky et al. 2015; Lim et al. 2018). Evtushevsky et al. (2019) also showed using reanalysis that the SH stratosphere connection to the central tropical Pacific has strengthened in recent decades in the austral spring. In this study, using reanalysis and multiple model ensembles with different greenhouse gas (GHG) and ozone-depleting substance (ODS) scenarios, we focus on austral winter ENSO, which allows the characterization of spring

and summer anomalies in the stratosphere (an important time period for stratosphere–troposphere coupling). Using multiple ensembles, we analyze ENSO's tropospheric teleconnections onto the SH eddy-driven jet under different GHG and ODS scenarios.

Here we aim to separate both a tropospheric and stratospheric pathway of ENSO onto SH austral spring and summer circulation, with a focus on spring. This complements the work done by Butler et al. (2014) for the NH, where both a tropospheric and stratospheric pathway of ENSO to the troposphere was identified during boreal autumn and winter. In that study, ENSO events of either polarity were found to be more likely to coincide with a sudden stratospheric warming (SSW). The stratospheric pathway was shown to affect climate over the North Atlantic and Eurasian region. Separation of the stratospheric and tropospheric pathways of ENSO is also discussed at length in Jiménez-Esteve and Domeisen (2018, 2020). However, as the SH stratosphere only rarely experiences SSWs, here we aim to investigate how ENSO variability affects both warm and cold SH polar stratospheres, and identify any differing effects from stratospheric and tropospheric pathways to SH tropospheric circulation.

## 2. Reanalysis and climate model ensembles

In this study we use reanalysis data as well as six different model ensembles encompassing two model frameworks, described below and in Table 1.

The model datasets are compared to a reanalysis assimilated by observations, specifically the JRA-55 global reanalysis (Kobayashi et al. 2015). This reanalysis's feature is its temporal coverage, extending from 1958 to the present, with years 1958–2019 used in this study. Monthly mean JRA-55 data are used at  $1.25^\circ$  latitude  $\times$   $1.25^\circ$  horizontal resolution on 37 pressure levels up to 1 hPa. It is important to note here that the earlier years 1958–79 (before the satellite era) in JRA-55 have substantially fewer assimilated observations, and therefore require more caution in their use. When comparing the analysis presented here to identical analysis over the satellite era of 1979–2019, very similar results are obtained. Therefore, we opted to use the full JRA-55 time series to reduce sampling uncertainty.

Four model ensembles with differing ozone-depleting substance (ODS) and greenhouse gas (GHG) concentrations (see Table 1) (Stone et al. 2018) were run using the high-top coupled chemistry–climate model Whole Atmosphere Community Climate Model (WACCM4), which is based on the Community Earth System Model, version 1 (CESM1), and is a fully coupled climate model that incorporates atmosphere, ocean, land, and sea ice modules (Marsh et al. 2013; Garcia et al. 2017). The setup of the model used here has a horizontal resolution of  $1.9^\circ$  latitude  $\times$   $2.5^\circ$  longitude and 66 vertical levels up to  $5.1 \times 10^{-6}$  hPa ( $\sim 140$  km). The chemical scheme used is the Model of Ozone and Related Tracers (MOZART) (Kinnison et al. 2007) and has been shown to accurately simulate polar ozone depletion and levels of chlorine reservoir species (Solomon et al. 2015, 2016). The ocean model is the

TABLE 1. Description of model ensembles and their forcings.

Model	Ensemble name	No. members	Time period used	GHGs	ODSs/ozone fields	Ocean	Model top
CESM1-WACCM(CAM4)	WACCM-GHG <sub>H</sub> ODS <sub>H</sub>	10	1995–2024	RCP 6.0 after 2005 (Meinshausen et al. 2011)	WMO 2011	POP2	66 levels with a top at $5.1 \times 10^{-6}$ hPa
CESM1-WACCM(CAM4)	WACCM-GHG <sub>L</sub> ODS <sub>L</sub>	10	1955–79	Historical	Historical	POP2	66 levels with a top at $5.1 \times 10^{-6}$ hPa
CESM1-WACCM(CAM4)	WACCM-GHG <sub>L</sub> ODS <sub>H</sub>	10	1995–2024	Fixed 1960 levels	WMO 2011	POP2	66 levels with a top at $5.1 \times 10^{-6}$ hPa
CESM1-WACCM(CAM4)	WACCM-GHG <sub>H</sub> ODS <sub>L</sub>	10	1995–2024	RCP 6.0 after 2005 (Meinshausen et al. 2011)	Fixed 1960 levels	POP2	66 levels with a top at $5.1 \times 10^{-6}$ hPa
CESM1(CAM5)	LENS	40	1995–2024	RCP 8.5 after 2005 (Meinshausen et al. 2011)	Prescribed zonally 4D fields from CESM1(WACCM) CMIP runs with a 10-yr running mean. See Kay et al. (2015) for details.	POP2	30 levels with a top at 3.64 hPa
CanESM2	CanESM2	50	1995–2024	RCP 8.5 after 2005, (Meinshausen et al. 2011)	Prescribed zonally symmetric ozone fields from modified SPARC dataset (Cionni et al. 2011)	NCOM 1.3 (Hurrell et al. 2013)	22 levels with a top at 1 hPa

Parallel Ocean Program (POP), version 2, and is fully coupled (therefore the ENSO events for each ensemble member are different). The setup used has a repeated cyclic 28-month quasi-biennial oscillation (QBO), no solar cycle or solar proton events, and updated sulfate area densities including twenty-first-century volcanic eruptions (Mills et al. 2016; Neely and Schmidt 2016). The four different WACCM ensembles employ different GHG and ODS forcings, with the naming scheme describing the relative forcings. They are all spun up from Chemistry Climate Model Initialization simulations beginning in 1955. Two simulations have evolving GHG and ODS concentrations, but over different time periods, WACCM-GHG<sub>H</sub>ODS<sub>H</sub> over 1995–2024 and WACCM-GHG<sub>L</sub>ODS<sub>L</sub> over 1955–79. The subscript letters L and H denote low or high GHG and ODS forcings, respectively, and are designed to be able to obtain the important differences of the WACCM ensembles directly from the title. The other two simulations are WACCM-GHG<sub>L</sub>ODS<sub>H</sub>, and WACCM-GHG<sub>H</sub>ODS<sub>L</sub>, both run over 1995–2024. WACCM-GHG<sub>L</sub>ODS<sub>H</sub> has fixed GHGs at 1960 levels and evolving ODSs, while WACCM-GHG<sub>H</sub>ODS<sub>L</sub> has fixed ODSs at 1960 levels and evolving GHGs. In WACCM-GHG<sub>H</sub>ODS<sub>L</sub>, the ODS<sub>L</sub> term differs from that in the WACCM-GHG<sub>L</sub>ODS<sub>L</sub> as it has evolving ODSs over 1955–79 compared to fixed ODSs at 1960 levels. The naming convention is the same as it is designed to convey relative ODS levels (see Table 1 for more information). The four ensembles each consist of 10 members, and are further classified in Table 1. Initialization of the

model ensemble members commences from slightly differing initial air temperatures, as is standard in such simulations (Kay et al. 2015; Solomon et al. 2017).

We also employ the CESM Large Ensemble (LENS), described in detail in Kay et al. (2015). The main difference of this ensemble as compared to WACCM is that it employs a lower model top of ~4 hPa with prescribed rather than coupled ozone fields (see Table 1 for details). In this study, we use all 40 members of LENS over the time period of 1995–2024, similar to the WACCM simulations described above. LENS also employs a prescribed QBO nudged to observed fields.

We also examine results from the CanESM2 model's “historical” dataset, which consists of 50 members. The model and its ensembles are described in detail in Arora et al. (2011) and Fyfe et al. (2017). This model is a spectral model with independent architectural structure to that of CESM. Similarly to LENS, CanESM2 has a relatively low top of 1 hPa and prescribed ozone fields (see Table 1). CanESM2 does not simulate or prescribe a QBO.

### 3. Methods

The ENSO index was calculated using principal component analysis of sea surface temperatures over the latitude–longitude range of 30°S–30°N and 140°–260°E. The first empirical orthogonal function (EOF) gives a representation of the eastern Pacific ENSO (hereafter referred to simply as ENSO). A June–August

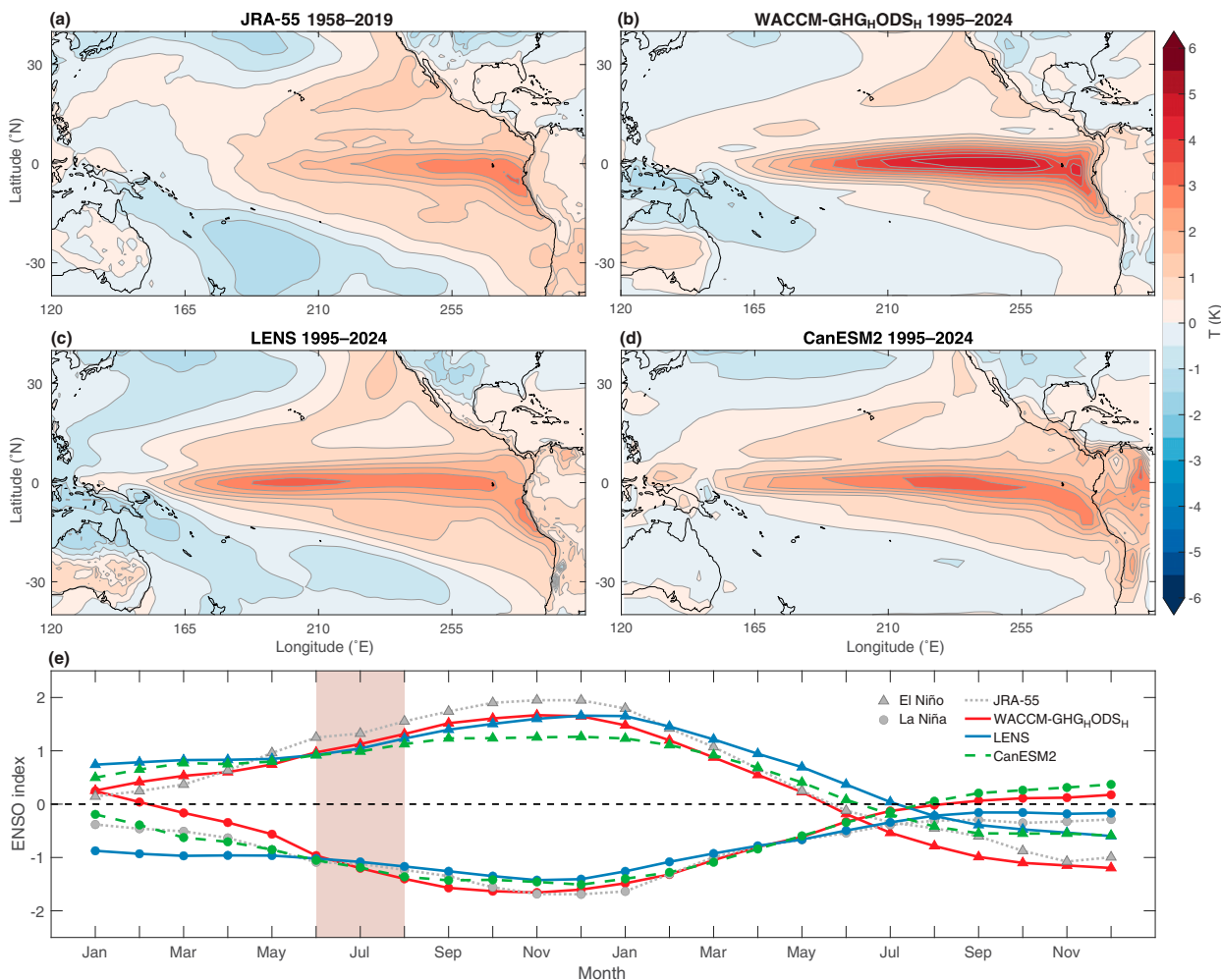


FIG. 1. June–August ENSO composite differences (El Niño – La Niña) of June–August surface temperatures for (a) JRA-55, (b) WACCM-GHG<sub>H</sub>ODS<sub>H</sub>, (c) LENS, and (d) CanESM2. (e) The seasonality of a June–August ENSO event. The shaded region indicates the months that were used in the construction of the seasonal ENSO index in this paper.

seasonal index is calculated by first forming monthly anomalies over the respective time periods. June–August seasonal averages are then calculated and linearly detrended. We next compute the EOFs over the ENSO latitude–longitude area described above by calculating the eigenvalues of the covariance matrix. The time period of June–August was chosen for two reasons: 1) A lag correlation analysis of monthly ENSO indices for the SH cold season from April to September shows that the anomalies are largest in the Antarctic polar stratosphere from a June ENSO in all model simulations, and August ENSO in JRA-55 (although the anomalies are still large in JRA-55 from June ENSO events). 2) ENSO events typically begin in austral winter and peak in austral summer before diminishing. Therefore, any austral winter ENSO events that disturb the SH stratosphere will also likely continue to strengthen into the summer. This means the SH troposphere will likely experience austral summer teleconnections from the same ENSO event that disturbed the stratosphere. Therefore, a June–August seasonal ENSO index was chosen.

Composite analysis of ENSO events was performed following Deser et al. (2017), by normalizing the seasonal ENSO index by its seasonal standard deviation. Then, any values above (below) 1 (–1) standard deviation are described as El Niño (La Niña) events. ENSO composite differences were calculated by first detrending the respective fields, with a linear breakpoint imposed in the year 2000 for both stratospheric and tropospheric fields to account for ozone recovery (this was not done for the WACCM-GHG<sub>H</sub>ODS<sub>L</sub> that did not have ozone depletion), then subtracting El Niño years from La Niña years. Significance of the ENSO composite differences is obtained using a two-tailed two-sample *t* test at the 95th or 90th percentile with sample sizes equal to the number of El Niño and La Niña events respectively.

Using this composite difference method described above, the surface temperature differences associated with a June–August ENSO in our analysis are shown in Fig. 1 for JRA-55, WACCM-GHG<sub>H</sub>ODS<sub>H</sub>, CanESM2, and LENS.

TABLE 2. Number of June–August El Niños and La Niñas that correspond to a warm or cold stratosphere within the region of 60°E–180° and 45°–75°S at 30 hPa during September and October.

	No. El Niños	No. La Niñas	No. El Niños and warm stratosphere	No. El Niños and cold stratosphere	No. La Niñas and warm stratosphere	No. La Niñas and cold stratosphere	No. neutral ENSO	No. warm stratosphere and neutral ENSO	No. cold stratosphere and neutral ENSO
JRA-55	7	12	0	3 (42.9%)	5 (41.7%)	0	43	8 (18.6%)	7 (16.3%)
WACCM-GHG <sub>H</sub> ODS <sub>H</sub>	51	49	2 (3.9%)	21 (41.2%)	11 (22.4%)	2 (4.1%)	200	38 (19.0%)	25 (12.5%)
WACCM-GHG <sub>H</sub> ODS <sub>L</sub>	47	45	2 (4.3%)	16 (34.0%)	10 (22.2%)	4 (8.9%)	208	35 (16.8%)	30 (14.4%)
WACCM-GHG <sub>L</sub> ODS <sub>H</sub>	56	50	1 (1.8%)	13 (23.2%)	13 (26.0%)	7 (14.0%)	194	25 (12.9%)	40 (20.1%)
WACCM-GHG <sub>L</sub> ODS <sub>L</sub>	44	42	2 (4.5%)	14 (31.8%)	8 (19.0%)	3 (7%)	164	30 (18.3%)	24 (14.6%)
CanESM2	222	240	21 (9.5%)	64 (28.8%)	57 (23.4%)	20 (8.3%)	1038	162 (15.6%)	139 (13.4%)
WACCM-combined	198	186	7 (3.5%)	64 (32.3%)	42 (22.6%)	16 (8.6%)	766	128 (16.75)	119 (15.5%)
All	427	438	28 (6.5%)	131 (30.7%)	104 (23.7%)	36 (8.2%)	1847	298 (16.1%)	265 (14.4%)

There is good representation of the ENSO structure in all ensembles compared to JRA-55. The most noticeable differences are that the WACCM-GHG<sub>H</sub>ODS<sub>H</sub> ensemble has a larger SST difference in the eastern Pacific compared to the reanalysis and the other models, and the location of largest SST difference in JRA-55 is concentrated farther eastward than the models, especially compared to LENS. Figure 1e also shows how the ENSO index progresses before and after the June–August ENSO index time period used in this study. Figure 1 shows that when a June–August ENSO event occurs, on average the event begins to strengthen in the early part of the year, and peaks late in the year and into the following year (i.e., peaks in austral summer before diminishing). This is consistent with the three different models and JRA-55, which gives confidence that the models are representing the seasonality of ENSO correctly.

Calculation of the eddy-driven jet stream location was performed by finding the latitude of maximum zonal wind between 70° and 40°S at 500 hPa. At this pressure level, separation of the eddy-driven and subtropical jets was easily performed by restricting the latitude range to these values. Eddy-driven jet stream analysis was also done at 850 hPa to make sure separation between the two jets was accurate. Otherwise, 850 hPa was not used here as much of the Antarctic surface is above this level. The latitude of the eddy-driven jet was smoothed using a moving mean of 20° in longitude.

To separate the influence of the tropospheric and stratospheric pathways of ENSO on tropospheric circulation changes, we first isolate the region where the largest stratospheric temperature perturbations associated with ENSO are located (i.e., within 60°–180°E, 75°–45°S at 30 hPa). Then, we identify any El Niño years that correspond to large temperature anomalies within that region of greater or less than 1 or –1 standard deviation during the September–October mean. The same approach is used for La Niña events (see Table S1 in the online supplemental material for a list of stratospheric

response years in JRA-55). This time period, pressure level, and latitude–longitude range were used as they give the best signal-to-noise ratio in WACCM and JRA-55. Better results for CanESM2 are obtained when using higher pressure levels, but for consistency 30 hPa is used. ENSO years that correspond to large Antarctic stratospheric changes are characterized as having a stratospheric response, hereafter referred to as the combined pathway, and ENSO years that do not correspond to large Antarctic stratospheric changes are characterized as having a passive stratospheric response, hereafter referred to as the tropospheric only pathway. El Niño and La Niña composite anomalies are computed as the difference from the entire climatology. Separating the ENSO events in this way allows for the evaluation of any ENSO stratospheric pathway (difference between combined and tropospheric only pathways) that may affect SH tropospheric circulation. See Table 2 for more information. Significance between subsets of data with and without a stratospheric pathway is shown at the 90th percentile following a two-sided *t* test.

## 4. Results

### a. Stratospheric composite differences

The late austral winter and early austral spring ENSO composite differences (El Niño minus La Niña) of stratospheric temperature are shown in Fig. 2 for JRA-55, WACCM-GHG<sub>H</sub>ODS<sub>H</sub>, LENS, and CanESM2. The high SH latitude composite differences at 10 hPa in August are largely negative and contained mostly within 0°–180°E, with smaller positive differences within 180°–300°E above the southeastern Pacific (Figs. 2a,d,g,j). For simplicity, here we are showing the composite differences between El Niño and La Niña years, instead of the El Niño and La Niña composite anomalies separately. For the most part, the SH stratospheric response to El Niño and La Niña are similar and opposite (see Figs. S1

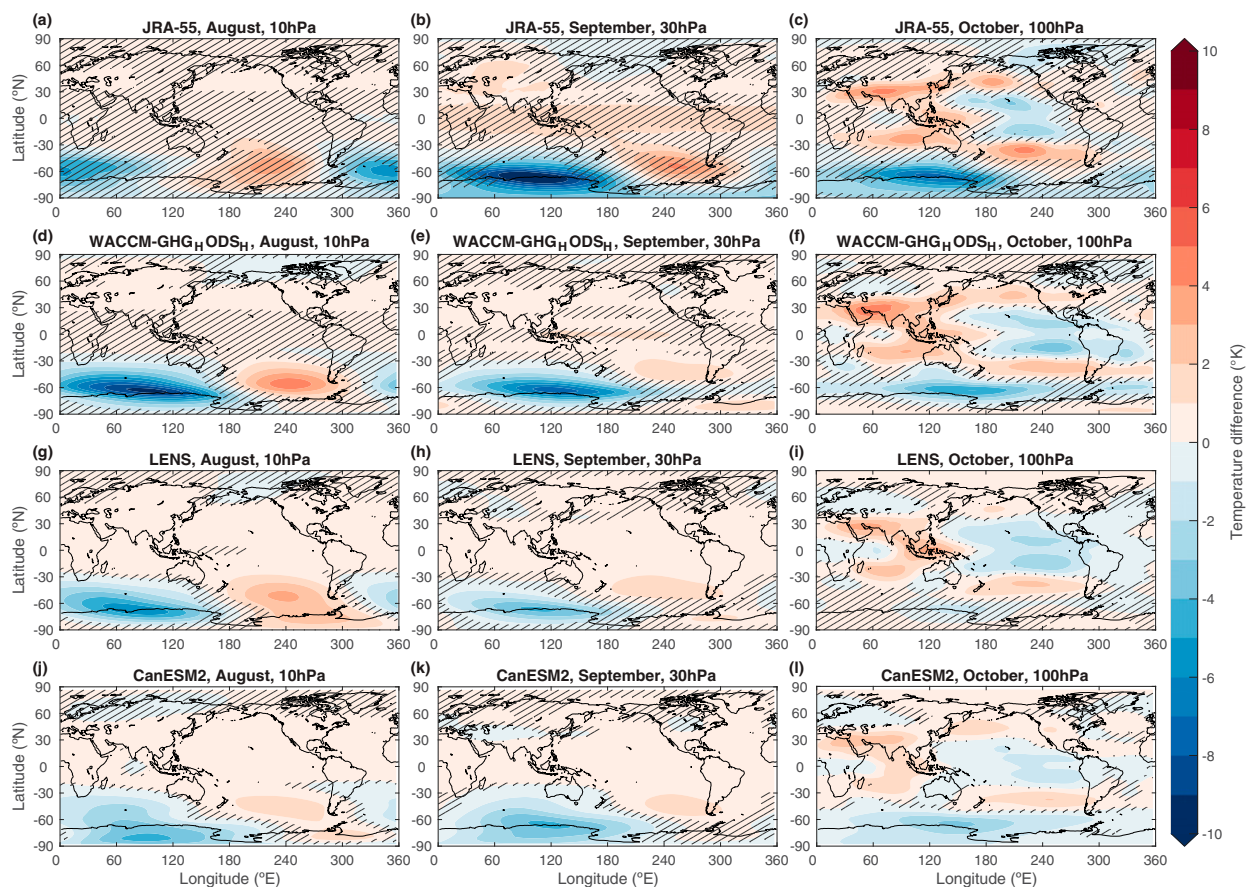


FIG. 2. June–August ENSO composite differences of August 10-hPa, September 30-hPa, and October 100-hPa temperatures for (a)–(c) JRA-55, (d)–(f) WACCM-GHG<sub>H</sub>ODS<sub>H</sub>, (g)–(i) LENS, and (j)–(l) CanESM2. Hatching shows where differences are not significantly different from each other ( $p < 0.05$ ) using a two-tailed  $t$  test.

and S2 for separation into El Niño and La Niña composite anomalies).

The largest differences occur in the WACCM-GHG<sub>H</sub>ODS<sub>H</sub> ensemble, of less than  $-9$  K, which compares to JRA-55 values of up to  $-7$  K. The anomalies are weaker in LENS and CanESM2 but the spatial structure of the anomalies is captured very well by all three ensembles. The anomalies are significant at the 95th percentile in the SH in JRA-55 and the different ensembles. The nature of these anomalies arises from both a change in the amplitude and the phase of the zonal wave 1, which is the dominant quasi-stationary wave in the stratosphere during austral spring (e.g., Waugh et al. 1999; Lin et al. 2009). During an El Niño, the zonal wave 1 has a smaller amplitude compared to a La Niña, especially near the wave maximum, and the phase is shifted eastward (see Fig. 7).

The anomalies descend and move eastward throughout the late winter and spring. During September (Figs. 2b,e,h,k), there is again excellent agreement of the structure of the anomalies between JRA-55 and the three ensembles, with high SH latitude negative anomalies at 30 hPa now mostly contained within  $60^{\circ}$ – $180^{\circ}$ E and much smaller positive anomalies within  $220^{\circ}$ – $300^{\circ}$ E. The differences are now largest in JRA-55, at nearly  $-9$  K. During October at 100 hPa (Figs.

2c,f,i,l), the anomalies are still present, and significant, in JRA-55, WACCM-GHG<sub>H</sub>ODS<sub>H</sub>, and CanESM2 (they are also present in ERA5 reanalysis, but not shown here). However, they are largely reduced in LENS. As an austral winter ENSO event likely precedes an austral summer ENSO event (Fig. 1e), and considering that ozone and temperature are strongly coupled in the stratosphere (Randel and Cobb 1994), these results are broadly consistent with the 6-month lag of total column ozone anomalies with ENSO presented in previous literature (Lin and Qian 2019; Evtushevsky et al. 2015). The vertical structure of these differences can be seen further in Fig. 3, which shows JRA-55 and WACCM-GHG<sub>H</sub>ODS<sub>H</sub> longitude–pressure plots averaged over  $45^{\circ}$ – $75^{\circ}$ S for individual months from August to November. The negative differences that are associated with El Niño in the lower stratosphere are accompanied by positive differences above. As the differences continue to descend through late spring and summer, these positive differences are found in the middle stratosphere, in agreement with Domeisen et al. (2019), and references therein.

The smaller magnitude of the LENS differences in October compared to JRA-55, WACCM-GHG<sub>H</sub>ODS<sub>H</sub>, and CanESM2 are most pronounced in the La Niña anomalies (Fig. S2), and could be due either to the LENS low top model

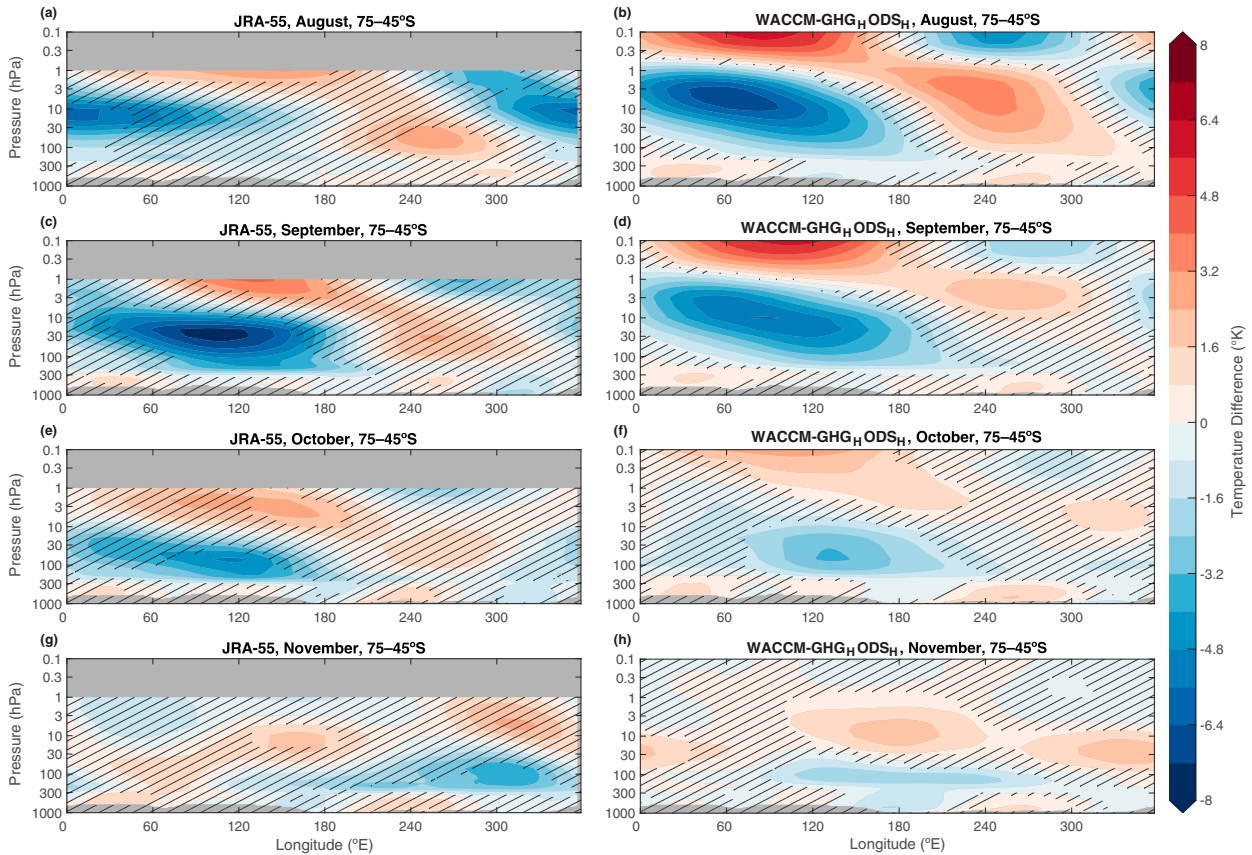


FIG. 3. Longitude–pressure ENSO composite differences of temperature for (left) JRA-55 and (right) WACCM-GHG<sub>H</sub>ODS<sub>H</sub> averaged over 45°–75°S. Four rows show results for August, September, October, and November. Hatching shows where differences are not significantly different from each other ( $p < 0.05$ ) using a two-tailed  $t$  test.

of ~4 hPa not properly representing the anomalies throughout the upper stratosphere and the mesosphere or to the prescribed ozone fields damping the anomaly signal during austral spring by having mismatched amplitudes and phases of the temperature and ozone zonal wave 1. This could occur because the temperature field is also influenced by dynamical drivers, such as ENSO. The differences could also be due to LENS having a much larger amplitude of the zonal wave 1 in the Antarctic stratosphere during spring compared to JRA-55, WACCM, and CanESM2 (see Fig. S3); however, further research is needed.

The composite differences seen in Fig. 2 for different models are also seen in the three other WACCM ensembles, shown in Fig. 4. There are some differences between the ensembles; for example, there is a larger difference (up to  $-6$  K larger) in WACCM-GHG<sub>H</sub>ODS<sub>H</sub> during August at 10 hPa and September at 30 hPa (Figs. 4a,b) compared to the other three ensembles, most noticeably WACCM-GHG<sub>L</sub>ODS<sub>H</sub> (Figs. 4g,h) and WACCM-GHG<sub>L</sub>ODS<sub>L</sub> (Figs. 4j,k), suggesting that the ENSO teleconnection onto the SH stratosphere may be stronger under enhanced GHG loading as these differences do lie outside the 95th percentile of 1000 sample bootstrapped variability (not shown). However, caution must be taken here as how ENSO and tropospheric ENSO teleconnections respond to

different GHGs scenarios is model-dependent (Yeh et al. 2018; Santoso et al. 2019; Cai et al. 2019).

The La Niña composite anomalies are strongest in August at 10 hPa in WACCM-GHG<sub>H</sub>ODS<sub>H</sub>, but are strongest in September at 30 hPa in the other three ensembles, indicating there may be large variability in the timing of the stratospheric teleconnection captured here between ensembles (see Figs. S4 and S5). There are also larger differences in WACCM-GHG<sub>H</sub>ODS<sub>H</sub> compared to WACCM-GHG<sub>H</sub>ODS<sub>L</sub> during October at 100 hPa, a time period and pressure level where ozone feedbacks onto temperature perturbations would take place. However, they are less significant.

These differences indicate that forcing changes may alter ENSO teleconnections into the SH stratosphere under different GHG and ODS scenarios. However, for the purposes of this paper, the main takeaway from Fig. 3 is that an SH stratospheric ENSO teleconnection is present, and is broadly consistent within the four different WACCM ensembles. It will therefore likely remain present into the near future as both GHG and ODS concentrations continue to change. Since the teleconnections are similar, later we combine the four WACCM ensembles to reduce sampling variability.

Table 2 breaks down, in more detail, the percentage of austral winter El Niño and La Niña events that are associated

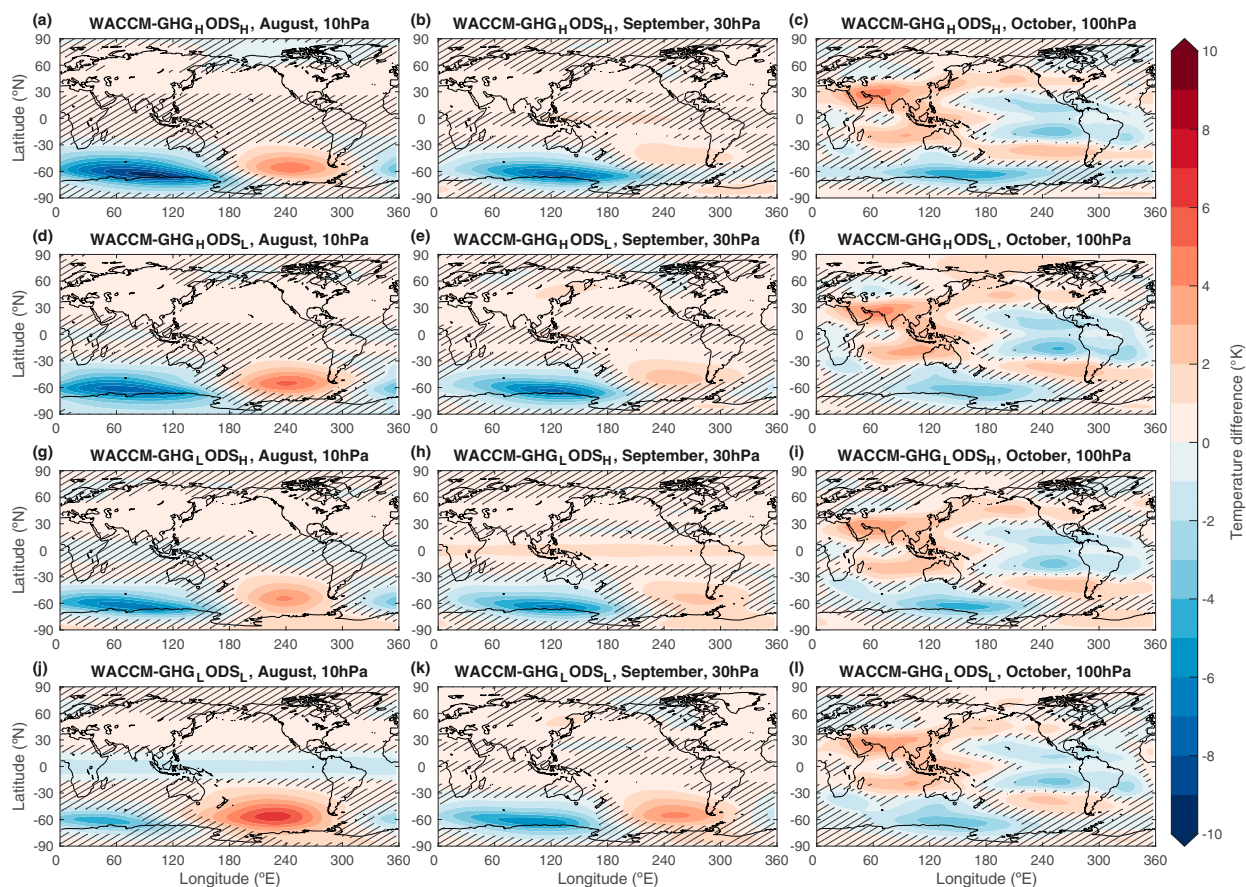


FIG. 4. June–August ENSO composite differences of August 10-hPa, September 30-hPa, and October 100-hPa temperatures for (a)–(c) WACCM-GHG<sub>H</sub>ODS<sub>H</sub>, (d)–(f) WACCM-GHG<sub>H</sub>ODS<sub>L</sub>, (g)–(i) WACCM-GHG<sub>L</sub>ODS<sub>H</sub>, and (j)–(l) WACCM-GHG<sub>L</sub>ODS<sub>L</sub>. Hatching shows where differences are not significantly different from each other ( $p < 0.05$ ) using a two-tailed  $t$  test.

with a warm or cold Antarctic stratosphere in September–October at 30 hPa within the region of  $60^{\circ}$ – $180^{\circ}$ E,  $45^{\circ}$ – $75^{\circ}$ S (above or below one standard deviation). LENS is omitted here due to the weaker stratospheric response to ENSO simulated in this ensemble (see Fig. 2). JRA-55 El Niños and La Niñas are associated with a cold or warm Antarctic stratosphere with an incident rate of 42.9% and 41.7% respectively. In contrast, the opposite (i.e., El Niño associated with a warm stratosphere) does not occur. These results are reflected in the model composites. Across all ensembles and JRA-55, the incident rates of El Niño associated with a warm or cold stratosphere are 6.5% and 30.7% respectively, while the incident rates of La Niña and a warm or cold stratosphere are 23.7% and 8.2% (see Fig. S6 for a scatterplot representation).

In the NH, Butler et al. (2014) showed that an SSW likely occurs during either an El Niño or La Niña winter. Here, in the SH, since SSWs are rare, we follow a different approach and investigate high and low temperature extremes. This produces a clear linear positive or negative temperature response of the stratosphere to the phase of ENSO (i.e., negative during El Niño and positive during La Niña).

The robustness of the August–October stratospheric differences (El Niño minus La Niña) associated with, and likely

forced by, the onset of ENSO events in the austral winter is seen to be different from a central Pacific El Niño response (e.g., Hurwitz et al. 2011), where the central Pacific El Niño response is associated with an Antarctic stratospheric temperature anomaly of opposite sign during November–December. Additionally, the downward progression of the anomalies seen in Fig. 3 raises a question: Do these anomalies influence SH tropospheric circulation during spring and summer? Such a relationship could occur since the differences are present in the lower stratosphere from September to November (see Fig. 3), a time period of known stratosphere–troposphere coupling (e.g., Lim et al. 2018), especially in the late spring, when the differences are at the same pressures and during the same time period as anthropogenic springtime Antarctic ozone depletion, which is well known to modulate the SAM in austral summer (e.g., Thompson and Solomon 2002). To investigate this, first we must establish the tropospheric ENSO teleconnection.

As ENSO events generally have peak strength in austral summer (Trenberth 1997) (Fig. 1e), the onset of ENSO events in austral winter is very likely to be followed by ENSO events through to summer. Therefore, it is likely that any spring and summer SH circulation changes in the troposphere associated

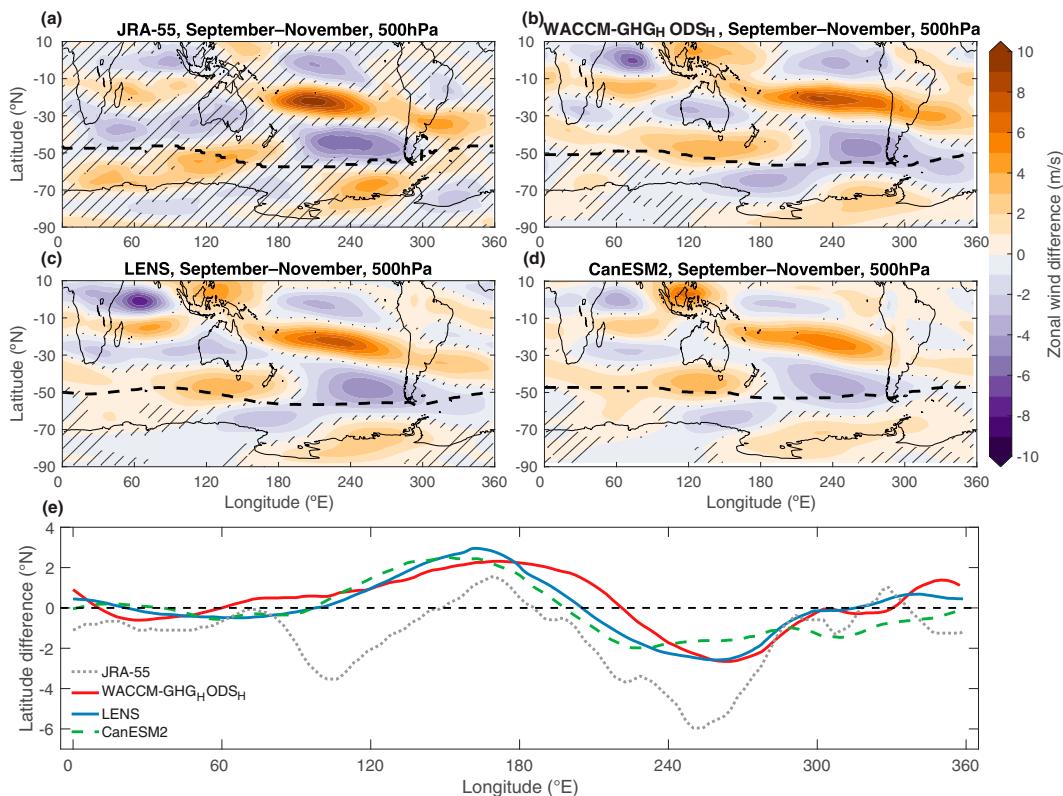


FIG. 5. June–August ENSO composite differences of September–November 500-hPa zonal wind for (a) JRA-55, (b) WACCM-GHG<sub>H</sub>ODS<sub>H</sub>, (c) LENS, and (d) CanESM2. Dashed black lines indicate the latitudes of maximum zonal wind. Hatching shows where differences are not significantly different from each other ( $p < 0.1$ ) using a two-tailed  $t$  test. (e) The ENSO composite difference of the latitudes of maximum zonal wind are shown as a function of longitude.

with the previous winter ENSO could be the result of the tropospheric ENSO teleconnection during spring and summer, and any downward propagation that may occur from the ENSO induced stratospheric anomalies could be hidden in these simultaneous teleconnections.

Additionally, any attempt to separate ENSO events by whether or not they are associated with a perturbed stratosphere may end up separating different subsets of ENSO events that have fundamentally different tropospheric teleconnections, and this may obscure any perceived downward influence of ENSO associated stratospheric anomalies. In the next sections, we show how JRA-55 and the ensembles represent these tropospheric teleconnections, and present a method for separating the stratospheric and tropospheric pathways of ENSO onto springtime SH tropospheric circulation, while carefully taking into account the above two concerns.

#### b. ENSO teleconnection onto the austral spring eddy jet

The teleconnections between ENSO variability during June–August and the SH circulation are investigated here in the zonal wind fields. Figure 5 shows the ENSO composite difference during austral spring 500-hPa zonal wind for JRA-55, WACCM-GHG<sub>H</sub>ODS<sub>H</sub>, LENS, and CanESM2. The

ENSO composite difference in the latitude of maximum zonal wind (used as a proxy for the eddy-driven jet location) is also shown. Similarly, to Figs. 2 and 3, here we are showing the composite differences for simplicity. The structure of the separate El Niño and La Niña composite anomalies are mostly opposite and similar. However, the magnitude of the El Niño teleconnection is slightly larger than the La Niña teleconnection in WACCM-GHG<sub>H</sub>ODS<sub>H</sub> and LENS, but not in CanESM2 and JRA-55. This can be seen in context of the stratospheric pathway in section 4c (see Figs. 8–10). During spring (Fig. 5), there is good agreement between the differences in JRA-55 and all ensembles. In WACCM-GHG<sub>H</sub>ODS<sub>H</sub>, LENS, and CanESM2, it is generally seen that there are positive differences equatorward of the average eddy-driven jet location (dashed black line) between 100° and 200°E, and negative differences equatorward between 180° and 300°E. In JRA-55, the composite difference pattern agrees well with the models, however, in the region from 0° to 180°E, the pattern is now located farther south in relation to the average location of the eddy-driven jet. During summer, JRA-55 also agrees very well with the three models, with a similar pattern compared to spring (see Fig. S7). Therefore, during the warm phase of ENSO, significant positive differences are seen equatorward of the average eddy-driven jet location within the 100°–200°E in the

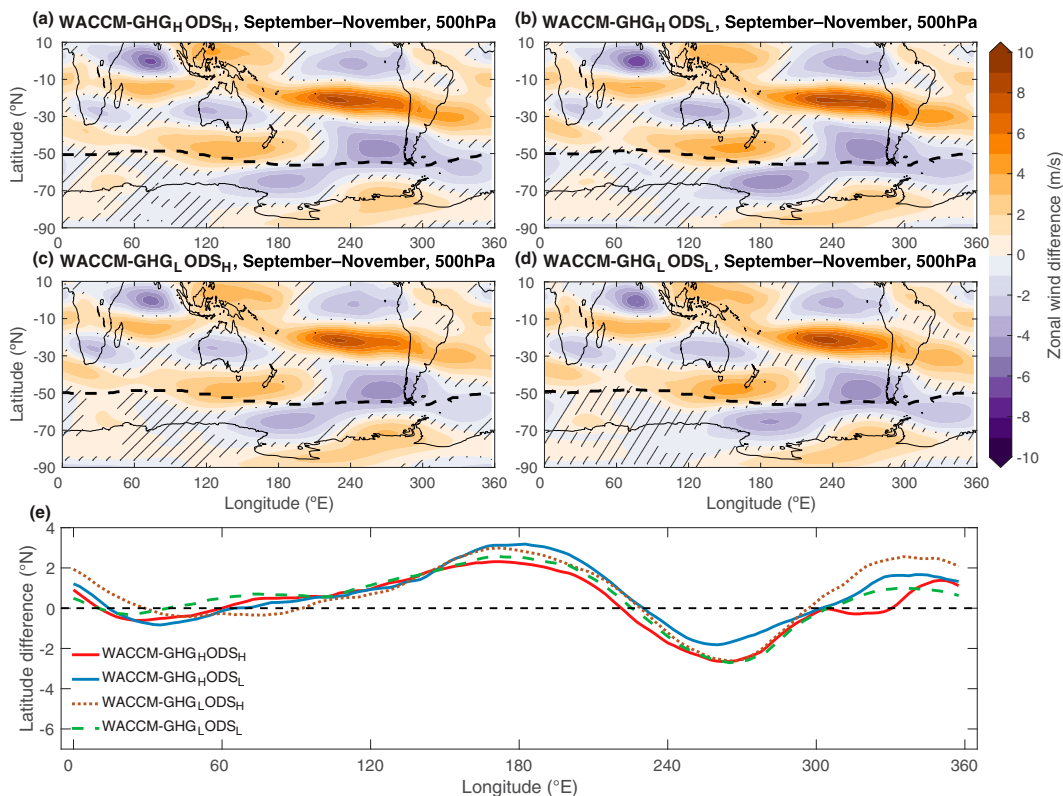


FIG. 6. June–August ENSO composite differences of September–November 500-hPa zonal wind for (a) WACCM-GHG<sub>H</sub>ODS<sub>H</sub>, (b) WACCM-GHG<sub>H</sub>ODS<sub>L</sub>, (c) WACCM-GHG<sub>L</sub>ODS<sub>H</sub>, and (d) WACCM-GHG<sub>L</sub>ODS<sub>L</sub>. Dashed lines indicate the latitudes of maximum zonal wind. Hatching shows where differences are not significantly different from each other ( $p < 0.1$ ) using a two-tailed  $t$  test. (e) The ENSO composite difference of the latitudes of maximum zonal wind as a function of longitude.

models ( $0^{\circ}$ – $180^{\circ}$ E and the South Atlantic during summer). This indicates stronger westerlies and therefore a more equatorward location of the eddy-driven jet during El Niño. In the southeast Pacific, significant positive differences are seen poleward of the average eddy-driven jet location in the models and JRA-55, indicating a more poleward location of the eddy-driven jet.

The ENSO composite difference in the eddy-driven jet location is captured in Fig. 5e where we see an equatorward shift in the jet between  $100^{\circ}$  and  $200^{\circ}$ E of around  $2^{\circ}$  latitude, and a poleward shift between  $200^{\circ}$  and  $300^{\circ}$ E in the models of around  $2^{\circ}$  latitude. There is reasonable agreement with JRA-55, except between  $90^{\circ}$  and  $150^{\circ}$ E, the jet teleconnection is shifted poleward. In summer (Fig. S7), we see an equatorward difference of the jet within  $0^{\circ}$ – $180^{\circ}$ E of around  $1^{\circ}$  latitude, with excellent agreement between the models and JRA-55. The peak in the equatorward difference between about  $100^{\circ}$  and  $200^{\circ}$ E where it is up to  $2^{\circ}$  latitude is the approximate location of the quasi-stationary southwestern Pacific anticyclone (Hobbs and Raphael 2010), and also agrees with Fogt et al. (2012) on regional variations in the SAM associated with ENSO. Farther east, over the southeastern Pacific the differences become negative, and are also very strong, up to  $-2^{\circ}$  latitude. This is the location of the quasi-stationary southeastern Pacific anticyclone. The differences return to a 0 in the

South Atlantic. Therefore, during spring, ENSO is negatively correlated to SAM between  $100^{\circ}$  and  $200^{\circ}$ E and positively correlated between  $200^{\circ}$  and  $300^{\circ}$ E, as an equatorward shift of the jet would indicate a negative SAM polarity. During the summer (Fig. S7) ENSO is negatively correlated to SAM everywhere except the southeastern Pacific ( $200^{\circ}$ – $300^{\circ}$ E), in agreement with previous studies (e.g., Fogt et al. 2012; L'Heureux and Thompson 2006; Lim et al. 2013). Therefore, it is clear there is regional structure to this correlation, especially in spring.

In JRA-55, the zonal wind differences in the SH have become significantly stronger at 500 hPa in recent years from 1979 onward (almost double that of the model simulations), whether this is due to recent years having stronger ENSO events (e.g., Lee and McPhaden 2010; Freund et al. 2019), or that there are better observations since 1979 requires further investigation. However, the longitudinal structures of the differences are the same when comparing the ENSO composite differences over 1958–2019 and 1979–2019 (not shown).

Figure 6 shows the ENSO composite differences of zonal wind and the eddy-driven jet stream under the different WACCM scenarios for the austral spring period. Since the composite differences are detrended and normalized to the mean, the direct ODS or GHG signal on the eddy-driven jet

is removed. Therefore, any significant differences in the ENSO teleconnection between WACCM ensembles will likely arise from either differences in the structure and intensity of ENSO, or nonlinearities in how ENSO projects onto SH tropospheric circulation under different GHG or ODS regimes. The zonal wind differences are very similar for the four different scenarios indicating that the teleconnection is consistent for different GHG and ODS loadings during spring. There are some larger differences in summer between scenarios, but they are not consistent when comparing to different CanESM2 ensembles one with only stratospheric ozone forcings, and one with preindustrial forcings (see Figs. S7 and S8). Therefore, the overall longitudinal structure of the teleconnection is very consistent between all models and ensembles, and will therefore likely remain consistent into the near future as GHG and ODS concentrations change. This gives confidence that any stratospheric–tropospheric teleconnection of ENSO onto SH tropospheric circulation will show similar features in all ensembles, and therefore combining the four different WACCM ensembles (hereafter referred to as WACCM-combined) to create a larger dataset is a reasonable approach going forward. This has the added benefit of producing a WACCM ensemble with similar ensemble members to CanESM2 (40 members compared to 50 members, respectively).

Here, we have established that the typical ENSO teleconnection onto the tropospheric eddy-driven jet in the SH is not longitudinally uniform in the separate model simulations, in agreement with previous literature (e.g., Fogt et al. 2012). In the next section, we aim to establish whether or not the stratospheric ENSO associated perturbations shown in Figs. 2, 3, and 4 exhibit stratosphere–troposphere coupling, thus providing an additional pathway for ENSO to affect SH tropospheric circulation.

### c. Downward propagation of ENSO-induced stratospheric anomalies

The key obstacle to separating the stratospheric expression of ENSO during austral spring and the tropospheric teleconnection is the strength of the tropospheric teleconnection. We first examine this by separating the austral winter ENSO years that exhibit a stratospheric springtime response in the SH from those that do not. The austral spring stratospheric differences are expected to impact tropospheric circulation as they occur during a key time period for stratosphere–troposphere coupling (Thompson et al. 2005; Lim et al. 2018). Different metrics of the two subsets of ENSO events are then compared: the stratospheric temperature differences, and the tropical Pacific surface temperature differences. If there are obvious differences in the structure of the surface temperatures (e.g., the location of largest SST differences is located in a different location, or is significantly stronger/weaker), then any differences in the tropospheric wind may just be due to different teleconnections from differing ENSO events. However, if the surface temperature differences are similar, then comparison of the composite anomalies in austral spring tropospheric circulation between these two subsets of data

provides an indication of how much the stratospheric ENSO pathway affects tropospheric circulation. If any stratospheric temperature biases existed in the model, they could potentially also affect the stratosphere–troposphere coupling. However, this is unlikely here due to the agreement between JRA-55 and the models in Figs. 2–4.

An austral spring stratospheric response to ENSO is characterized here by a large September–October temperature anomaly [greater (less) than 1 (–1) standard deviation] at 30 hPa within the region of 60°–180°E, 75°–45°S (i.e., the region of largest anomalies; see Figs. 2 and 4). The anomalies are not biased against either an El Niño or La Niña. For example, all El Niño years that have either a positive or negative temperature anomaly exceeding 1 standard deviation within the region are included in the subset of ENSO years with a combined pathway. This ensures that both positive and negative stratospheric extremes are sampled for both phases of ENSO. The remaining years are characterized as ENSO events with a tropospheric only pathway. This methodology is performed for the WACCM-combined and CanESM2 ensembles, and JRA-55. See the methods section (section 3) for more details. The numbers of coincident El Niño and La Niña years displaying temperature extremes within the described region are shown in Table 2. The number of stratospheric extremes that occur during neutral ENSO years are also tabulated.

Figure 7 shows the differences between the combined pathway and tropospheric only pathway subsets of ENSO events for WACCM-combined. Figures 7a and 7b show September–October temperatures averaged over 75°–45°S at 30 hPa. For the tropospheric only pathway (Fig. 7a), we see that the El Niño and La Niña years have similar temperatures compared to climatology (black dotted line). While, when there is a combined pathway (Fig. 7b), by definition, there is a stratospheric response. Figure 7b shows that the majority of warm temperature anomalies occur during a La Niña, and the majority of cold temperature anomalies occur during an El Niño.

Figures 7c and 7d show the lower stratospheric October temperature responses to the two different subsets of ENSO events. For the tropospheric only pathway, the negative temperature difference that is seen in Figs. 2 and 3 all but disappears, and when there is a combined pathway, the negative difference is enhanced. Therefore, when there is a combined pathway, we would expect a circulation response in the troposphere, compared to the tropospheric only pathway, to have similar structure to that of ozone depletion (i.e., a zonal shift in the tropospheric eddy-driven jet; this is investigated in Figs. 8–11). To make sure the circulation differences are not due to sampling two subsets of ENSO events that are distinctly different, Figs. 7e and 7f show the austral spring surface temperature composite differences for the two separate datasets. The figures show that the two different subsets of ENSO events are very similar in structure and intensity and are not significantly different from each other, giving confidence that the difference in the tropospheric composites between the two subsets of data is arising from stratosphere/troposphere coupling. See Figs. S10 and S11 for the corresponding figure for JRA-55 and CanESM2.

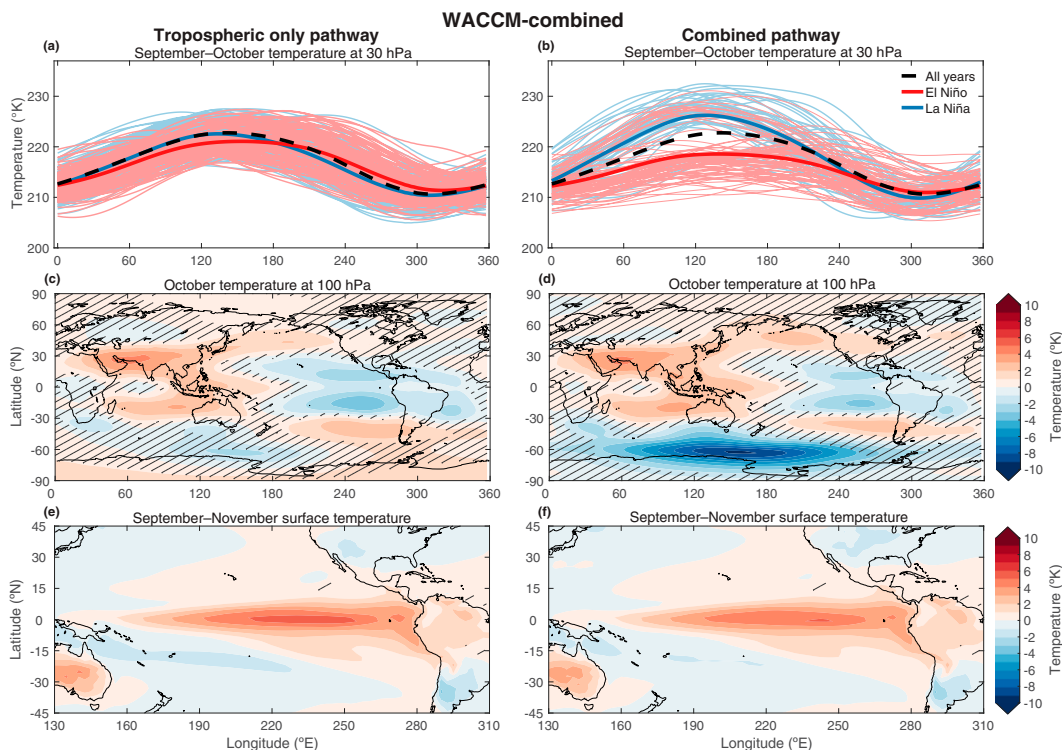


FIG. 7. Separation of June–August ENSO events that (b) have and (a) do not have an austral spring stratospheric response between  $75^{\circ}$ – $45^{\circ}$ S and  $60^{\circ}$ – $180^{\circ}$ E in WACCM-combined. (c),(d) The ENSO composite differences of October 100-hPa temperatures are shown for the two subsets of ENSO years, and (e),(f) similarly September–November surface temperature. For (a)–(d), hatching shows where differences are not significantly different from each other ( $p < 0.1$ ) using a two-tailed  $t$  test. For (e) and (f), hatching shows where the composite differences in (e) are significantly different from (f).

To establish what effect the stratospheric extremes shown in Fig. 7 would have on the tropospheric circulation during austral spring and summer, Fig. 8 shows the 500-hPa zonal wind response to composite warm and cold Antarctic stratospheres that occur during a neutral ENSO year. This is done for JRA-55, CanESM2, and WACCM-combined. Figures 8g and 8h show the WACCM difference due to ozone depletion for both austral spring and summer (difference between WACCM-GHG<sub>H</sub>ODS<sub>H</sub> and WACCM-GHG<sub>H</sub>ODS<sub>L</sub>, and includes all ENSO and ENSO-neutral years).

It is clear that when there is a warm Antarctic stratosphere in September–October during an ENSO-neutral year (Fig. 8), we see negative 500-hPa zonal wind anomalies near  $60^{\circ}$ S and positive anomalies near  $45^{\circ}$ S. This is seen in JRA-55, CanESM2, and WACCM-combined. The opposite is seen when there is a cold Antarctic stratosphere, but with a slightly smaller magnitude compared to when there is a warm Antarctic stratosphere. Compared to the anomalies caused by ozone depletion in WACCM during spring (Fig. 8g), the anomalies during the cold phase are of similar magnitude and the anomalies during the warm phase are slightly larger. However, comparing to austral summer when the ozone influence on the troposphere is greatest, the anomalies are approximately half during the cold phase and the same during the warm phase.

Next, we show the austral spring 500-hPa zonal wind response for the combined pathway, the tropospheric only pathway, and the difference between the two. This is done for the El Niño (Fig. 9) and La Niña (Fig. 10) composites. Here we have separated El Niño and La Niña, instead of conducting a composite difference, to compare with the neutral ENSO years (Fig. 8).

For the JRA-55 El Niño composite during austral spring (Fig. 9), the difference (Fig. 9c) between the combined pathway (Fig. 9a) and tropospheric only pathway (Fig. 9b) for 500-hPa zonal wind represents the stratospheric pathway and shows a pattern that is shifted poleward compared to Fig. 8b (neutral ENSO with cold stratosphere). Therefore, in this case, we see little agreement with CanESM2 (Fig. 9f) and WACCM-combined (Fig. 9i), which show positive (negative) anomalies south (north) of the climatological eddy-driven jet and good agreement with Figs. 8c and 8b. This indicates a poleward shift of the eddy-driven jet due to a El Niño associated cold Antarctic stratosphere. It is important to note here that the number of El Niño years available in JRA-55 is a likely reason for any differences between JRA-55 and the model ensembles, which is also clearly seen in the limited significance seen in the JRA-55 composite anomalies (Figs. 9a,b) and the differences between the two (Fig. 9c). However, for

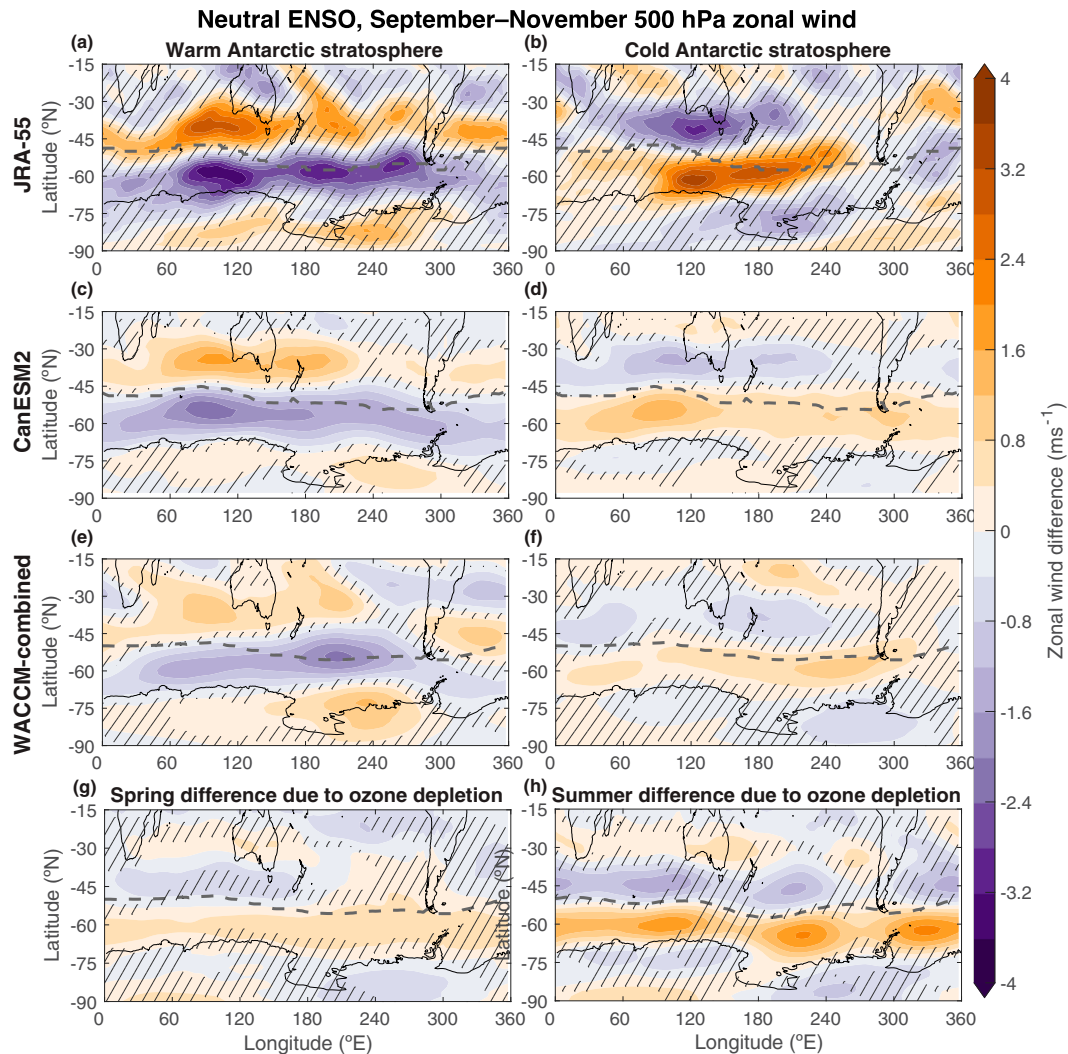


FIG. 8. September–November 500-hPa zonal wind response to Antarctic stratospheric extremes that occur during a neutral June–August ENSO for (a),(b) JRA-55, (c),(d) CanESM2, and (e),(f) WACCM-combined. (g),(h) Ozone hole depletion influence through the difference between the WACCM-GHG<sub>H</sub>ODS<sub>H</sub> and WACCM-GHG<sub>H</sub>ODS<sub>L</sub> ensembles for spring and summer respectively. Dashed lines indicate the latitudes of climatological maximum zonal wind. Hatching shows where differences are not significantly different from each other ( $p < 0.1$ ) using a two-tailed  $t$  test.

La Niña (Fig. 10), the JRA-55 500-hPa zonal wind difference (Fig. 10c) is very clear and in agreement with both CanESM2 (Fig. 10f) and WACCM-combined (Fig. 10i) and with Figs. 8a, 8c, and 8e. WACCM-combined and CanESM2 also show the strongest response during a La Niña, consistent with Figs. 8a, 8c, and 8e. Therefore, the most significant stratospheric connection of ENSO onto SH circulation is seen during La Niña. This is most notably in austral spring, but it also occurs in austral summer, but the signal is slightly weaker and less significant (see Figs. S12 and S13). However, this is expected considering the stratospheric anomalies peak in the early spring.

Comparing to Fig. 8h, we see that the stratospheric pathway of ENSO onto the austral spring zonal wind is approximately half of what is seen due to ozone depletion during austral

summer in WACCM for both an El Niño–induced cold stratosphere (Fig. 9i) and an La Niña–induced warm stratosphere (Fig. 10i). This brings into context by how much, compared to ozone depletion, an ENSO year that has a stratospheric pathway differs from an ENSO year that does not.

Figures 9 and 10 also highlight that the tropospheric pathway [panels (b), (e), and (h)] to El Niño and La Niña are not zonally uniform, in agreement with Figs. 5 and 6. Meanwhile, the stratospheric pathway [panels (c), (f), and (i)] of El Niño and La Niña are more zonally uniform (especially in CanESM2 and WACCM-combined) and opposite to that of the tropospheric pathway between 100° and 200°E and of the same sign between 200° and 300°E in austral spring (in austral summer, the stratospheric pathway is opposite everywhere

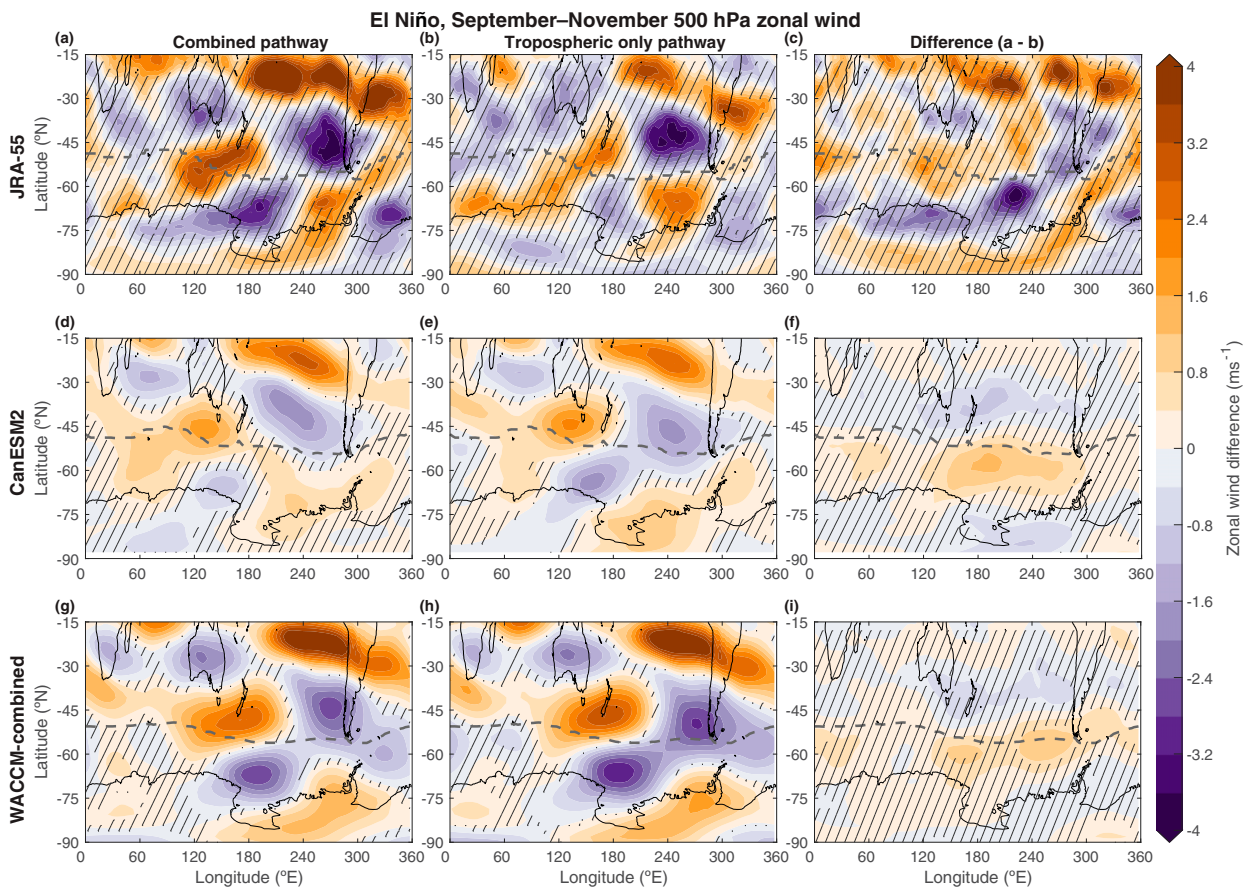


FIG. 9. 500-hPa zonal wind El Niño composite anomalies for subsets: combined and tropospheric only pathways (see Fig. 7) during September–November for JRA-55, CanESM2, and WACCM-combined. Dashed lines indicate the latitudes of climatological maximum zonal wind. Hatching shows where differences are not significantly different from each other ( $p < 0.1$ ) using a two-tailed  $t$  test.

except 200°–300°S). Additionally, the stratospheric pathway is slightly weaker compared to the tropospheric pathway in the models. Therefore, even though the stratospheric pathway is clearly present, it is not the major driver of SH ENSO teleconnections in the troposphere, but instead plays a secondary role.

Using large ensembles (50 members for CanESM2, and 40 members for WACCM-combined) allows us to investigate the large variability in the stratospheric pathway on tropospheric circulation. An example of this is shown in Fig. 11. Here, significance from a two-sided two-sample  $t$  test for the zonal mean difference at 60°S is shown as a function of the number of ensemble members used. This was calculated by bootstrapping 1000 times the difference between the tropospheric only and combined pathways for different numbers of ensemble members used and taking the average  $p$  value. For La Niña, we need approximately 12 members for WACCM-combined and 22 members for CanESM2 to achieve a zonal average difference that is significant at the 90th percentile. However, for El Niño we need around 35 members for WACCM-combined and 50 members for CanESM2 (more regional significance at 60°S requires fewer ensemble members, as can be inferred from Figs. 9 and 10). This further indicates that the influence

of the stratospheric pathway on tropospheric circulation is stronger and more significant during a La Niña.

## 5. Conclusions

The far-reaching global implications of ENSO have been studied extensively, from impacts on precipitation in Australia and the Americas to an ENSO stratospheric pathway onto the NH surface. Here, we have presented evidence for a novel connection, an ENSO stratospheric pathway onto SH circulation during the austral summer. The SH teleconnections act as a pathway to the surface through stratosphere–troposphere coupling.

We investigate the effects of austral winter ENSO, calculated as the first principal component of tropical Pacific surface temperatures, on the SH stratosphere with JRA-55 reanalysis, and six model ensembles using three different global climate models: CESM1 WACCM4, CESM1 LENS, and the CanESM2 models.

All model ensembles and JRA-55 display large late austral winter and austral spring stratospheric anomalies associated with austral winter ENSO events. This is defined by large

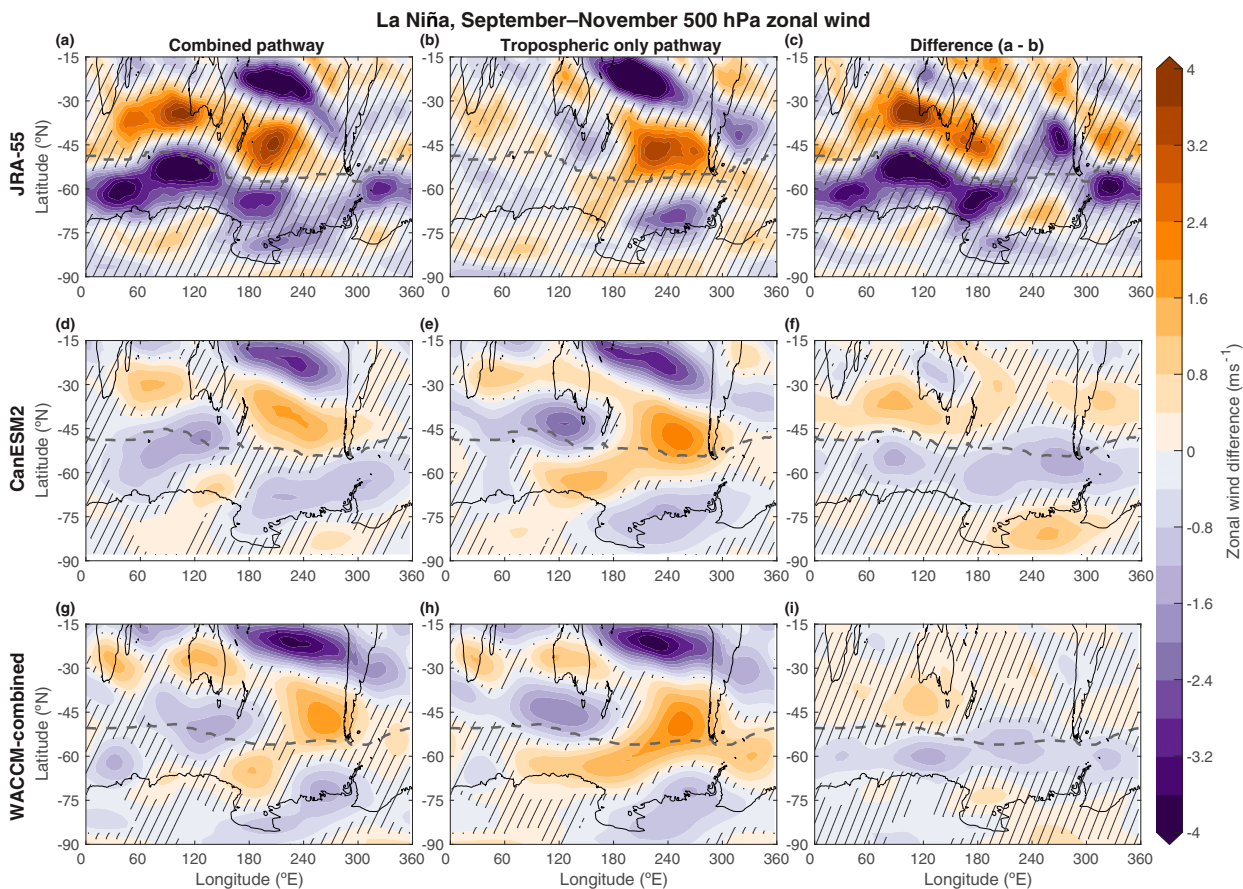


FIG. 10. As in Fig. 9, but for September–November La Niña composite anomalies.

negative composite differences in temperature (El Niño minus La Niña) throughout the high-latitude SH stratosphere within  $0^{\circ}$ – $180^{\circ}$ E, and smaller positive anomalies within  $180^{\circ}$ – $300^{\circ}$ E, a clear modulation of the zonal wave 1, in agreement with other recent studies (Lin and Qian 2019), but in general of opposite sign of the response to a central Pacific El Niño (e.g., Hurwitz et al. 2011). The differences arise as early as August, peaking around 10 hPa and near  $60^{\circ}$ S, but extending as low as 100 hPa. Over the following months, the peak differences descend through the stratosphere into the middle and lower polar stratosphere, causing large disturbances of up to  $-8$  K in JRA-55 and  $-5$  K in WACCM, at 100 hPa in October, and causing consistent lower stratospheric differences from August to October, a key time for stratosphere–troposphere coupling. This teleconnection is consistent among all model ensembles and JRA-55 in August, September, and October, with the exception of LENS in October, which shows much smaller anomalies in the lower stratosphere. The lack of a consistent signal in LENS as the anomalies descend throughout the spring is likely not due to a low top model or prescribed ozone, since CanESM2 retains the anomalies; it may be due to overly large wave amplitudes in LENS obscuring the signal.

Comparison of different WACCM ensembles shows that even though there are some differences in the strength of the

signal, it is consistent under different GHG and ODS scenarios, indicating that it will remain into the near future as GHG and ODS concentrations change. There is some evidence that high GHG loading may be acting to enhance the ENSO signal in the SH austral stratosphere, especially during an August El Niño at 10 hPa. It is less clear how high ODS loading modulates the signal, with only small differences seen in October at 100 hPa. However, how ENSO and ENSO teleconnections respond to different GHGs scenarios are model-dependent and have not reached an intermodel consensus (Yeh et al. 2018; Santoso et al. 2019; Cai et al. 2019).

The SH austral spring and summer eddy-driven jet locations are linked to ENSO, with an equatorward shift occurring during an El Niño over the  $100^{\circ}$ – $200^{\circ}$ E and a poleward shift occurring between  $200^{\circ}$  and  $300^{\circ}$ E during spring. During summer the equatorward shifts extend from  $0^{\circ}$  to  $200^{\circ}$ E and the South Atlantic. This indicates that its relationship to the SAM is not zonally symmetric, in agreement with previous work (e.g., Fogt et al. 2012; Lim et al. 2013).

By separating ENSO events that instigate large SH stratospheric temperature anomalies from those that do not and comparing to SH stratospheric temperature anomalies that occur during neutral-ENSO events, we have established that an ENSO stratospheric pathway onto the SH eddy-driven jet

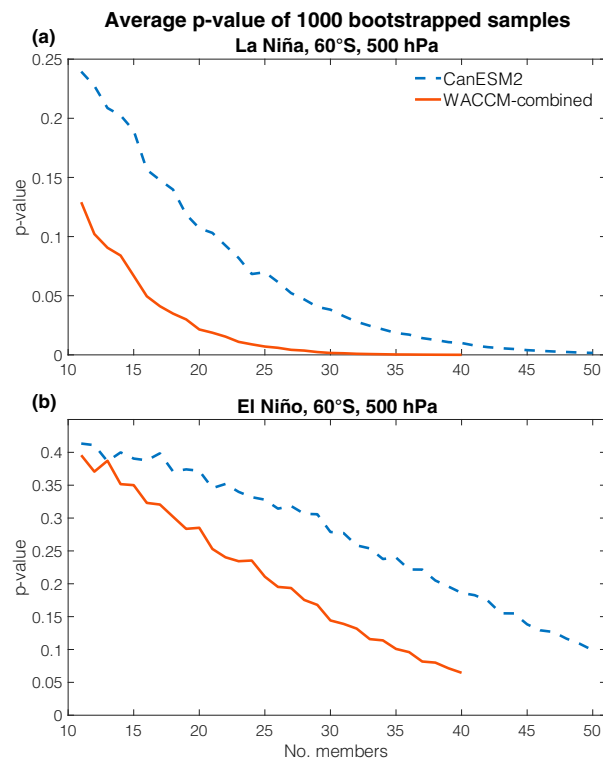


FIG. 11. Average  $p$  values for the number of ensemble members used to calculate the difference between the combined and tropospheric only pathways after a 1000 bootstrap process of random members within the 40-member pool for WACCM-combined and 50-member pool for CanESM2. The  $p$  values were calculated from a two-sided  $t$  test between the two datasets, corresponding to Figs. 9f,i and 10f,i.

exists during austral spring and summer. This result is robust among CanESM2, and in a combination of the WACCM ensembles for both La Niña and El Niño events. JRA-55 reanalysis shows good agreement with the model ensembles for La Niña during spring and summer, but there is an inconsistent response for El Niño events in JRA-55 during spring. However, both the WACCM and CanESM2 stratospheric pathways are also most significant during La Niña compared to El Niño, and a large number of ensemble members are needed to obtain significance at the 90th percentile for El Niño events. This is also consistent with the tropospheric response being larger during a neutral-ENSO warm stratosphere compared to a cold stratosphere in JRA-55 and the models (Fig. 8).

In the NH, Butler et al. (2014) showed that it is common for SSWs to occur during both a La Niña and an El Niño. This teleconnection to the stratosphere results in a different tropospheric response to ENSO due to the downward influence of the SSW in boreal winter, resulting in an ENSO stratospheric pathway to the NH troposphere. The method used here is not directly comparable to Butler et al. (2014), since SSWs are rare in the SH. However, it is clear that an El Niño event has a different impact than a La Niña event in the

SH stratosphere. Therefore, the tropospheric expression of the stratospheric anomaly depends largely on the phase of ENSO. An austral winter El Niño will more likely cause a cold, more stable Antarctic stratosphere, which strengthens the spring and summer polar vortex and shifts the jet stream poleward. In contrast, an austral winter La Niña will more likely cause a warm, less stable stratosphere, which weakens the polar vortex and shifts the jet stream equatorward.

In addition to what Evtushevsky et al. (2019) reported for austral spring, our results show that when the stratospheric pathway is present, the forcing from the stratospheric anomalies is likely of opposite sign to the tropospheric teleconnection over 100°–200°E during spring (0°–200°E during summer). This results in a smaller equatorward/poleward shift of the jet stream compared to El Niño/La Niña years that do not have a stratospheric response. The opposite occurs in the southeastern Pacific (200°–300°E), where the stratospheric and tropospheric teleconnections are of the same sign, resulting in larger poleward/equatorward differences of the jet stream in the presence of El Niño/La Niña associated stratospheric anomalies. The magnitude of the stratospheric pathway is smaller than the tropospheric pathway and is therefore only playing a secondary role in how ENSO affects the tropospheric circulation. For context, the strength of the stratospheric pathway in the models is approximately half of that caused by Antarctic ozone depletion in austral summer. Even though the stratospheric pathway is slightly weaker compared to the tropospheric pathway, it could have meaningful impacts on rainfall and temperature associated with eddy-driven jet driven weather fronts during ENSO events.

Therefore, the stratospheric pathway of ENSO presented here is important for understanding the connection between ENSO and SH circulation anomalies during austral summer, and also for understanding to what extent a particular ENSO event may affect regional climate in the SH.

*Acknowledgments.* K.S. and S. S. were supported by a gift to MIT from an anonymous donor and by a grant from the National Science Foundation NSF 1848863. D. W. J. T. is supported by NSF AGS-1848785. This research was enabled by the computational and storage resources of NCAR's Computational and Information Systems Laboratory (CISL), sponsored by the NSF. D. E. K. was partly supported by NSF FESD-1338814. Cheyenne: HPE/SGI ICE XA System (NCAR Community Computing, Boulder, CO, National Center for Atmospheric Research, doi:10.5065/D6RX99HX). We acknowledge Environment and Climate Change Canada's Canadian Centre for Climate Modelling and Analysis for executing and making available the CanESM2 large ensemble simulations, and the Canadian Sea Ice and Snow Evolution (CanSISE) Network for proposing the simulations. The JRA-55 dataset used in this study is from the Japanese 55-year Reanalysis project carried out by the Japan Meteorological Agency (JMA).

*Data availability statement.* WACCM model results shown in this paper are available online here: [https://acomstaff.acom.ucar.edu/dkin/JClim\\_Stone\\_2021/](https://acomstaff.acom.ucar.edu/dkin/JClim_Stone_2021/). LENS model results are publicly

available here: <https://www.cesm.ucar.edu/projects/community-projects/LENS/data-sets.html>. CanESM2 model results are publicly available here: <http://crd-data-donnees-rdc.ec.gc.ca/CCCMA/products/CanSISE/output/CCCma/CanESM2/>. JRA-55 data are available here: <https://rda.ucar.edu/datasets/ds628.1/>.

## REFERENCES

- Arblaster, J. M., and G. A. Meehl, 2006: Contributions of external forcings to southern annular mode trends. *J. Climate*, **19**, 2896–2905, <https://doi.org/10.1175/JCLI3774.1>.
- Arora, V. K., and Coauthors, 2011: Carbon emission limits required to satisfy future representative concentration pathways of greenhouse gases. *Geophys. Res. Lett.*, **38**, L05805, <https://doi.org/10.1029/2010GL046270>.
- Bjerknes, J., 1969: Atmospheric teleconnections from the equatorial Pacific 1. *Mon. Wea. Rev.*, **97**, 163–172, [https://doi.org/10.1175/1520-0493\(1969\)097<0163:ATFTEP>2.3.CO;2](https://doi.org/10.1175/1520-0493(1969)097<0163:ATFTEP>2.3.CO;2).
- Butler, A. H., L. M. Polvani, and C. Deser, 2014: Separating the stratospheric and tropospheric pathways of El Niño–Southern Oscillation teleconnections. *Environ. Res. Lett.*, **9**, 024014, <https://doi.org/10.1088/1748-9326/9/2/024014>.
- Cai, W., and Coauthors, 2019: Pantropical climate interactions. *Science*, **363**, eaav4236, <https://doi.org/10.1126/science.aav4236>.
- Cionni, I., and Coauthors, 2011: Ozone database in support of CMIP5 simulations: Results and corresponding radiative forcing. *Atmos. Chem. Phys.*, **11**, 11 267–11 292, <https://doi.org/10.5194/acp-11-11267-2011>.
- Deser, C., I. R. Simpson, K. A. McKinnon, and A. S. Phillips, 2017: The Northern Hemisphere extratropical atmospheric circulation response to ENSO: How well do we know it and how do we evaluate models accordingly? *J. Climate*, **30**, 5059–5082, <https://doi.org/10.1175/JCLI-D-16-0844.1>.
- Domeisen, D. I. V., C. I. Garfinkel, and A. H. Butler, 2019: The teleconnection of El Niño Southern Oscillation to the stratosphere. *Rev. Geophys.*, **57**, 5–47, <https://doi.org/10.1029/2018RG000596>.
- Evtushevsky, O. M., V. O. Kravchenko, L. L. Hood, and G. P. Milinevsky, 2015: Teleconnection between the central tropical Pacific and the Antarctic stratosphere: Spatial patterns and time lags. *Climate Dyn.*, **44**, 1841–1855, <https://doi.org/10.1007/s00382-014-2375-2>.
- , A. V. Grytsai, and G. P. Milinevsky, 2019: Decadal changes in the central tropical Pacific teleconnection to the Southern Hemisphere extratropics. *Climate Dyn.*, **52**, 4027–4055, <https://doi.org/10.1007/s00382-018-4354-5>.
- Fogt, R. L., D. H. Bromwich, and K. M. Hines, 2011: Understanding the SAM influence on the South Pacific ENSO teleconnection. *Climate Dyn.*, **36**, 1555–1576, <https://doi.org/10.1007/s00382-010-0905-0>.
- , J. M. Jones, and J. Renwick, 2012: Seasonal zonal asymmetries in the southern annular mode and their impact on regional temperature anomalies. *J. Climate*, **25**, 6253–6270, <https://doi.org/10.1175/JCLI-D-11-00474.1>.
- Freund, M. B., B. J. Henley, D. J. Karoly, H. V. McGregor, N. J. Abram, and D. Dommenges, 2019: Higher frequency of Central Pacific El Niño events in recent decades relative to past centuries. *Nat. Geosci.*, **12**, 450–455, <https://doi.org/10.1038/s41561-019-0353-3>.
- Fyfe, J. C., and Coauthors, 2017: Large near-term projected snowpack loss over the western United States. *Nat. Commun.*, **8**, 14996, <https://doi.org/10.1038/ncomms14996>.
- García, R. R., A. K. Smith, D. E. Kinnison, Á. de la Cámara, and D. J. Murphy, 2017: Modification of the gravity wave parameterization in the Whole Atmosphere Community Climate Model: Motivation and results. *J. Atmos. Sci.*, **74**, 275–291, <https://doi.org/10.1175/JAS-D-16-0104.1>.
- Garreaud, R. D., and D. S. Battisti, 1999: Interannual (ENSO) and interdecadal (ENSO-like) variability in the Southern Hemisphere tropospheric circulation. *J. Climate*, **12**, 2113–2123, [https://doi.org/10.1175/1520-0442\(1999\)012<2113:IEAIEL>2.0.CO;2](https://doi.org/10.1175/1520-0442(1999)012<2113:IEAIEL>2.0.CO;2).
- Grimm, A. M., and R. G. Tedeschi, 2009: ENSO and extreme rainfall events in South America. *J. Climate*, **22**, 1589–1609, <https://doi.org/10.1175/2008JCLI2429.1>.
- Hartmann, D. L., and F. Lo, 1998: Wave-driven zonal flow vacillation in the Southern Hemisphere. *J. Atmos. Sci.*, **55**, 1303–1315, [https://doi.org/10.1175/1520-0469\(1998\)055<1303:WDZ FVI>2.0.CO;2](https://doi.org/10.1175/1520-0469(1998)055<1303:WDZ FVI>2.0.CO;2).
- Hobbs, W. R., and M. N. Raphael, 2010: Characterizing the zonally asymmetric component of the SH circulation. *Climate Dyn.*, **35**, 859–873, <https://doi.org/10.1007/s00382-009-0663-z>.
- Horel, J. D., and J. M. Wallace, 1981: Planetary-scale atmospheric phenomena associated with the Southern Oscillation. *Mon. Wea. Rev.*, **109**, 813–829, [https://doi.org/10.1175/1520-0493\(1981\)109<0813:PSAPAW>2.0.CO;2](https://doi.org/10.1175/1520-0493(1981)109<0813:PSAPAW>2.0.CO;2).
- Hurrell, J. W., and Coauthors, 2013: The Community Earth System Model: A framework for collaborative research. *Bull. Amer. Meteor. Soc.*, **94**, 1339–1360, <https://doi.org/10.1175/BAMS-D-12-00121.1>.
- Hurwitz, M. M., P. A. Newman, L. D. Oman, and A. M. Molod, 2011: Response of the Antarctic stratosphere to two types of El Niño events. *J. Atmos. Sci.*, **68**, 812–822, <https://doi.org/10.1175/2011JAS3606.1>.
- Irving, D., and I. Simmonds, 2016: A new method for identifying the Pacific–South American pattern and its influence on regional climate variability. *J. Climate*, **29**, 6109–6125, <https://doi.org/10.1175/JCLI-D-15-0843.1>.
- Jiménez-Esteve, B., and D. I. V. Domeisen, 2018: The tropospheric pathway of the ENSO–North Atlantic teleconnection. *J. Climate*, **31**, 4563–4584, <https://doi.org/10.1175/JCLI-D-17-0716.1>.
- , and —, 2020: Nonlinearity in the tropospheric pathway of ENSO to the North Atlantic. *Wea. Climate Dyn.*, **1**, 225–245, <https://doi.org/10.5194/wcd-1-225-2020>.
- Karoly, D. J., 1989: Southern Hemisphere circulation features associated with El Niño–Southern Oscillation events. *J. Climate*, **2**, 1239–1252, [https://doi.org/10.1175/1520-0442\(1989\)002<1239:SHCFAW>2.0.CO;2](https://doi.org/10.1175/1520-0442(1989)002<1239:SHCFAW>2.0.CO;2).
- , 1990: The role of transient eddies in low-frequency zonal variations of the Southern Hemisphere circulation. *Tellus*, **42A**, 41–50, <https://doi.org/10.3402/tellusa.v42i1.11858>.
- Kay, J. E., and Coauthors, 2015: The Community Earth System Model (CESM) large ensemble project: A community resource for studying climate change in the presence of internal climate variability. *Bull. Amer. Meteor. Soc.*, **96**, 1333–1349, <https://doi.org/10.1175/BAMS-D-13-00255.1>.
- Kidson, J. W., 1988: Indices of the Southern Hemisphere zonal wind. *J. Climate*, **1**, 183–194, [https://doi.org/10.1175/1520-0442\(1988\)001<0183:IOTSHZ>2.0.CO;2](https://doi.org/10.1175/1520-0442(1988)001<0183:IOTSHZ>2.0.CO;2).
- , and M. R. Sinclair, 1995: The influence of persistent anomalies on Southern Hemisphere storm tracks. *J. Climate*, **8**, 1938–1950, [https://doi.org/10.1175/1520-0442\(1995\)008<1938:TIOPAO>2.0.CO;2](https://doi.org/10.1175/1520-0442(1995)008<1938:TIOPAO>2.0.CO;2).

- Kim, B. M., H. Choi, S. J. Kim, and W. Choi, 2017: Amplitude-dependent relationship between the southern annular mode and the El Niño Southern Oscillation in austral summer. *Asia-Pac. J. Atmos. Sci.*, **53**, 85–100, <https://doi.org/10.1007/s13143-017-0007-6>.
- King, A. D., M. G. Donat, L. V. Alexander, and D. J. Karoly, 2015: The ENSO–Australian rainfall teleconnection in reanalysis and CMIP5. *Climate Dyn.*, **44**, 2623–2635, <https://doi.org/10.1007/s00382-014-2159-8>.
- Kinnison, D. E., and Coauthors, 2007: Sensitivity of chemical tracers to meteorological parameters in the MOZART-3 chemical transport model. *J. Geophys. Res.*, **112**, D20302, <https://doi.org/10.1029/2006JD007879>.
- Kobayashi, S., and Coauthors, 2015: The JRA-55 reanalysis: General specifications and basic characteristics. *J. Meteor. Soc. Japan*, **93**, 5–48, <https://doi.org/10.2151/jmsj.2015-001>.
- Lee, T., and M. J. McPhaden, 2010: Increasing intensity of El Niño in the central-equatorial Pacific. *Geophys. Res. Lett.*, **37**, L14603, <https://doi.org/10.1029/2010GL044007>.
- L'Heureux, M. L., and D. W. J. Thompson, 2006: Observed relationships between the El Niño–Southern Oscillation and the extratropical zonal-mean circulation. *J. Climate*, **19**, 276–287, <https://doi.org/10.1175/JCLI3617.1>.
- Lim, E. P., H. H. Hendon, and H. Rashid, 2013: Seasonal predictability of the southern annular mode due to its association with ENSO. *J. Climate*, **26**, 8037–8054, <https://doi.org/10.1175/JCLI-D-13-00006.1>.
- , —, and D. W. J. Thompson, 2018: Seasonal evolution of stratosphere–troposphere coupling in the Southern Hemisphere and implications for the predictability of surface climate. *J. Geophys. Res. Atmos.*, **123**, 12 002–12 016, <https://doi.org/10.1029/2018JD029321>.
- Lin, J., and T. Qian, 2019: Impacts of the ENSO lifecycle on stratospheric ozone and temperature. *Geophys. Res. Lett.*, **46**, 10 646–10 658, <https://doi.org/10.1029/2019GL083697>.
- Lin, P., Q. Fu, S. Solomon, and J. M. Wallace, 2009: Temperature trend patterns in Southern Hemisphere high latitudes: Novel indicators of stratospheric change. *J. Climate*, **22**, 6325–6341, <https://doi.org/10.1175/2009JCLI2971.1>.
- Lindzen, R. S., and S. Nigam, 1987: On the role of sea surface temperature gradients in forcing low-level winds and convergence in the tropics. *J. Atmos. Sci.*, **44**, 2418–2436, [https://doi.org/10.1175/1520-0469\(1987\)044<2418:OTROSS>2.0.CO;2](https://doi.org/10.1175/1520-0469(1987)044<2418:OTROSS>2.0.CO;2).
- Liu, Z., and M. Alexander, 2007: Atmospheric bridge, oceanic tunnel, and global climatic teleconnections. *Rev. Geophys.*, **45**, RG2005, <https://doi.org/10.1029/2005RG000172>.
- Lorenz, D. J., and D. L. Hartmann, 2001: Eddy–zonal flow feedback in the Southern Hemisphere. *J. Atmos. Sci.*, **58**, 3312–3327, [https://doi.org/10.1175/1520-0469\(2001\)058<3312:EZFFIT>2.0.CO;2](https://doi.org/10.1175/1520-0469(2001)058<3312:EZFFIT>2.0.CO;2).
- Marsh, D. R., M. J. Mills, D. E. Kinnison, J.-F. Lamarque, N. Calvo, and L. M. Polvani, 2013: Climate change from 1850 to 2005 simulated in CESM1(WACCM). *J. Climate*, **26**, 7372–7391, <https://doi.org/10.1175/JCLI-D-12-00558.1>.
- McBride, J. L., and N. Nicholls, 1983: Seasonal relationships between Australian rainfall and the Southern Oscillation. *Mon. Wea. Rev.*, **111**, 1998–2004, [https://doi.org/10.1175/1520-0493\(1983\)111<1998:SRBARA>2.0.CO;2](https://doi.org/10.1175/1520-0493(1983)111<1998:SRBARA>2.0.CO;2).
- McIntyre, M. E., and N. T. Palmer, 1983: Breaking planetary waves in the stratosphere. *Nature*, **305**, 593–600, <https://doi.org/10.1038/305593a0>.
- Meinshausen, M., and Coauthors, 2011: The RCP greenhouse gas concentrations and their extensions from 1765 to 2300. *Climatic Change*, **109**, 213–241, <https://doi.org/10.1007/s10584-011-0156-z>.
- Mills, M. J., and Coauthors, 2016: Global volcanic aerosol properties derived from emissions, 1990–2014, using CESM1 (WACCM). *J. Geophys. Res. Atmos.*, **121**, 2332–2348, <https://doi.org/10.1002/2015JD024290>.
- Mo, K. C., and G. Ghil, 1987: Statistics and dynamics of persistent anomalies. *J. Atmos. Sci.*, **44**, 877–902, [https://doi.org/10.1175/1520-0469\(1987\)044<0877:SADOPA>2.0.CO;2](https://doi.org/10.1175/1520-0469(1987)044<0877:SADOPA>2.0.CO;2).
- , and J. N. Paegle, 2001: The Pacific–South American modes their downstream affects. *Int. J. Climatol.*, **21**, 1211–1229, <https://doi.org/10.1002/joc.685>.
- Neely, R. R., and A. Schmidt, 2016: VolcanEESM: Global volcanic sulphur dioxide (SO<sub>2</sub>) emissions database from 1850 to present—Version 1.0. Centre for Environmental Data Analysis, accessed 4 Feb 2016, <https://doi.org/10.5285/76ebdc0b-0eed-4f70-b89e-55e606bcd568>.
- Polvani, L. M., D. W. Waugh, G. J. P. Correa, and S. W. Son, 2011: Stratospheric ozone depletion: The main driver of twentieth-century atmospheric circulation changes in the Southern Hemisphere. *J. Climate*, **24**, 795–812, <https://doi.org/10.1175/2010JCLI3772.1>.
- Randel, W. J., and J. B. Cobb, 1994: Coherent variations of monthly mean total ozone and lower stratospheric temperature. *J. Geophys. Res.*, **99**, 5433–5447, <https://doi.org/10.1029/93JD03454>.
- Rasmusson, E. M., and T. H. Carpenter, 1982: Variations in tropical sea surface temperature and surface wind fields associated with Southern Oscillation/El Niño. *Mon. Wea. Rev.*, **110**, 354–384, [https://doi.org/10.1175/1520-0493\(1982\)110<0354:VITSST>2.0.CO;2](https://doi.org/10.1175/1520-0493(1982)110<0354:VITSST>2.0.CO;2).
- Renwick, J. A., 1998: ENSO-related variability in the frequency of South Pacific blocking. *Mon. Wea. Rev.*, **126**, 3117–3123, [https://doi.org/10.1175/1520-0493\(1998\)126<3117:ERVITF>2.0.CO;2](https://doi.org/10.1175/1520-0493(1998)126<3117:ERVITF>2.0.CO;2).
- , and M. J. Revell, 1999: Blocking over the South Pacific and Rossby wave propagation. *Mon. Wea. Rev.*, **127**, 2233–2247, [https://doi.org/10.1175/1520-0493\(1999\)127<2233:BOTSPA>2.0.CO;2](https://doi.org/10.1175/1520-0493(1999)127<2233:BOTSPA>2.0.CO;2).
- Ropelewski, C. F., and M. S. Halpert, 1986: North American precipitation and temperature patterns associated with the El Niño/Southern Oscillation (ENSO). *Mon. Wea. Rev.*, **114**, 2352–2362, [https://doi.org/10.1175/1520-0493\(1986\)114<2352:NAPATP>2.0.CO;2](https://doi.org/10.1175/1520-0493(1986)114<2352:NAPATP>2.0.CO;2).
- Santoso, A., and Coauthors, 2019: Dynamics and predictability of El Niño–Southern Oscillation: An Australian perspective on progress and challenges. *Bull. Amer. Meteor. Soc.*, **100**, 403–420, <https://doi.org/10.1175/BAMS-D-18-0057.1>.
- Seager, R., N. Harnik, Y. Kushnir, W. Robinson, and J. Miller, 2003: Mechanisms of hemispherically symmetric climate variability. *J. Climate*, **16**, 2960–2978, [https://doi.org/10.1175/1520-0442\(2003\)016<2960:MOHSCV>2.0.CO;2](https://doi.org/10.1175/1520-0442(2003)016<2960:MOHSCV>2.0.CO;2).
- Simpson, I. R., T. G. Shepherd, and M. Sigmond, 2011: Dynamics of the lower stratospheric circulation response to ENSO. *J. Atmos. Sci.*, **68**, 2537–2556, <https://doi.org/10.1175/JAS-D-11-05.1>.
- Solomon, S., D. Kinnison, J. Bandoro, and R. Garcia, 2015: Simulation of polar ozone depletion: An update. *J. Geophys. Res. Atmos.*, **120**, 7958–7974, <https://doi.org/10.1002/2015JD023365>.
- , D. J. Ivy, D. Kinnison, M. J. Mills, R. R. Neely, and A. Schmidt, 2016: Emergence of healing in the Antarctic ozone layer. *Science*, **310**, 307–310, <https://doi.org/10.1126/science.aee0061>.
- , and Coauthors, 2017: Mirrored changes in Antarctic ozone and stratospheric temperature in the late 20th versus early

- 21st centuries. *J. Geophys. Res. Atmos.*, **122**, 8940–8950, <https://doi.org/10.1002/2017JD026719>.
- Son, S. W., N. F. Tandon, L. M. Polvani, and D. W. Waugh, 2009: Ozone hole and Southern Hemisphere climate change. *Geophys. Res. Lett.*, **36**, L15705, <https://doi.org/10.1029/2009GL038671>.
- Stone, K. A., S. Solomon, and D. E. Kinnison, 2018: On the identification of ozone recovery. *Geophys. Res. Lett.*, **45**, 5158–5165, <https://doi.org/10.1029/2018GL077955>.
- Thompson, D. W. J., and J. M. Wallace, 2000: Annular mode in the extratropical circulation. Part I: Month-to-month variability. *J. Climate*, **13**, 1000–1016, [https://doi.org/10.1175/1520-0442\(2000\)013<1000:AMITEC>2.0.CO;2](https://doi.org/10.1175/1520-0442(2000)013<1000:AMITEC>2.0.CO;2).
- , and S. Solomon, 2002: Interpretation of recent Southern Hemisphere climate change. *Science*, **296**, 895–899, <https://doi.org/10.1126/science.1069270>.
- , —, and M. P. Baldwin, 2005: Stratosphere–troposphere coupling in the Southern Hemisphere. *J. Atmos. Sci.*, **62**, 708–715, <https://doi.org/10.1175/JAS-3321.1>.
- , —, P. J. Kushner, M. H. England, K. M. Grise, and D. J. Karoly, 2011: Signatures of the Antarctic ozone hole in Southern Hemisphere surface climate change. *Nat. Geosci.*, **4**, 741–749, <https://doi.org/10.1038/ngeo1296>.
- Trenberth, K. E., 1984: Signal versus noise in the Southern Oscillation. *Mon. Wea. Rev.*, **112**, 326–332, [https://doi.org/10.1175/1520-0493\(1984\)112<0326:SVNITS>2.0.CO;2](https://doi.org/10.1175/1520-0493(1984)112<0326:SVNITS>2.0.CO;2).
- , 1997: The definition of El Niño. *Bull. Amer. Meteor. Soc.*, **78**, 2771–2777, [https://doi.org/10.1175/1520-0477\(1997\)078<2771:TDOENO>2.0.CO;2](https://doi.org/10.1175/1520-0477(1997)078<2771:TDOENO>2.0.CO;2).
- Wang, L., P. J. Kushner, and D. W. Waugh, 2013: Southern Hemisphere stationary wave response to changes of ozone and greenhouse gases. *J. Climate*, **26**, 10205–10217, <https://doi.org/10.1175/JCLI-D-13-00160.1>.
- Waugh, D. W., W. J. Randel, S. Pawson, P. A. Newman, and E. R. Nash, 1999: Persistence of the lower stratospheric polar vortices. *J. Geophys. Res.*, **104**, 27 191–27 201, <https://doi.org/10.1029/1999JD900795>.
- WMO, 2011: Scientific Assessment of Ozone Depletion: 2010. WMO 52, 516 pp.
- Wyrтки, K., 1975: El Niño—The dynamic response of the equatorial Pacific Ocean to atmospheric forcing. *J. Phys. Oceanogr.*, **5**, 572–584, [https://doi.org/10.1175/1520-0485\(1975\)005<0572:ENTDRO>2.0.CO;2](https://doi.org/10.1175/1520-0485(1975)005<0572:ENTDRO>2.0.CO;2).
- Yang, C., T. Li, X. Dou, and X. Xue, 2015: Signal of central Pacific El Niño in the Southern Hemispheric stratosphere during austral spring. *J. Geophys. Res. Atmos.*, **120**, 11 438–11 450, <https://doi.org/10.1002/2015JD023486>.
- Yeh, S. W., and Coauthors, 2018: ENSO atmospheric teleconnections and their response to greenhouse gas forcing. *Rev. Geophys.*, **56**, 185–206, <https://doi.org/10.1002/2017RG000568>.